submitted to *Geophys. J. Int.*

A Method for the Prediction of Seismic Discontinuity Topography from Thermochemical Mantle Circulation Models

Gwynfor T. Morgan[1], J. Huw Davies[1], Robert Myhill[2], James Wookey[2] and James Panton[1,

[1] *School of Earth and Environmental Sciences, Cardiff University, Cardiff, United Kingdom*

[2] *School of Earth Sciences, University of Bristol, Bristol, United Kingdom*

[3] *now at Institut für Geophysik und Meteorologie, Universität zu Köln*

SUMMARY

We demonstrate a method for the prediction of seismic discontinuity topography from thermochemical Mantle Circulation Models (MCMs). We find the discontinuity depth by using the peak reflectivity at each location in our mid-mantle, taking account of compositional as well as thermal variations. We make some comparisons of our predicted topographies with those observed using SS-precursors, developing a simple smoothing filter to capture the distribution of sensitivity of a published topography model – finding that such filtering has a significant impact on the predicted discontinuity topographies. We also consider the significance of lateral variations in reflectivity or reflection amplitude in our predicted datasets and the real Earth. Finally, we consider what aspects of mid-mantle discontinuity structure would be matched by the predicted discontinuity structure from an Earth-like MCM – particularly the mean depths of the discontinuities, the amplitude of the topography and the shape of its spherical harmonic spectra.

Key words: Mantle Transition Zone, Seismic Discontinuities, SS precursors

1 INTRODUCTION

Discontinuities in the material properties of the Earth's mantle are a long-standing feature of 1D seismological models (e.g. Jeffreys & Bullen, 1940) and for over 75 years have been associated with phase transitions (e.g. Birch, 1952), where the stable material phase changes due to increasing pressure. In the mid-mantle the principal discontinuities around 410 and 660 km depth (hereafter referred to as 'd410' and 'd660') are usually associated with the reactions $Ol\,(\mathrm{Olivine}) \rightarrow Wd\,(\mathrm{Wadsleyite})$ (e.g. Ringwood & Major, 1970) and $Rw\,(\mathrm{Ringwoodite}) \rightarrow Brm\,(\mathrm{Bridgmanite}) + Pc\,(\mathrm{Periclase})$ (e.g. Ito et al., 1984).

Topography on d410 and d660 was first recognised in the early 1990s (e.g. Revenaugh & Jordan, 1991; Shearer & Masters, 1992), using ScS reverberations and SdS underside reflections (SS precursors). Since then, many global studies have been published, principally using SS precursors (e.g. Flanagan & Shearer, 1998; Gu et al., 1998, 2003; Lawrence & Shearer, 2008; Houser et al., 2008; Houser & Williams, 2010; Houser, 2016; Yu et al., 2017; Huang et al., 2019; Guo & Zhou, 2020; Waszek et al., 2021b) as well as a larger number of contributions using Receiver Function methods in regions with a high density of seismic stations (e.g., Chevrot et al., 1999; Collier & Helffrich, 2001; Thompson et al., 2011; Lee et al., 2014; Cottaar & Deuss, 2016; Maguire et al., 2018; Keifer & Dueker, 2019; Rao et al., 2020; Yu et al., 2020; Agius et al., 2021; Liu et al., 2023; Burky et al., 2023; Bonatto et al., 2024; Glasgow et al., 2024). Global studies have converged on peak-to-peak topography amplitude on the order of ~ 40km on both discontinuities, and a strong positive correlation between the depths of d410 and d660 (e.g., Houser & Williams, 2010). This last observation runs counter to the expected anticorrelation from the opposing Clapeyron slopes of the olivine-out and ringwoodite-out reactions. Explanations have included (i) The 3D nature of mantle thermal structure (e.g. Shearer & Masters, 1992; Goes et al., 2022), (ii) compositional variations (e.g. Houser et al., 2008), (iii) a positive Clapeyron slope at high temperatures controlling d600 (e.g. Houser & Williams, 2010; Waszek et al., 2021b) and (iv) the presence of water changing phase diagrams (although this is considered unlikely by seismologists and mineral physicists (Houser, 2016; Muir et al., 2021)) have all been suggested – but there is not yet a clear consensus in the seismological, mineral physics or geodynamic communities on the cause of this positive d410-d660 correlation. SdS topographies are typically corrected for crustal structure (which might advance or delay the SS phase compared to a global average, meaning that a discontinuity is interpreted as shallower or deeper than it is actually) using the model CRUST 1.0 or its predecessors

(Laske et al., 2012); however the lithosphere also has an extremely heterogeneous structure (e.g., Pasyanos et al., 2014) which is not usually corrected for – this could also explain the positive d410-d660 correlation (e.g. Tauzin et al., 2022).

As the topographies of d410 and d660 are recognised as being dominantly controlled by temperature, there is a long-standing understanding that it should be possible to invert the depths of the discontinuities and their topography for the average and range of mid-mantle temperatures. Shearer & Masters (1992) estimated a temperature range at $660\ \mathrm{km}$ depth of between $300-600\mathrm{K}$ based on a simple calculation from their observed topography and contemporary estimates of the Clapeyron slope of the post-spinel reaction. However, subsequent workers (e.g. Deuss et al., 2006) showed that the d660 could not be understood simply using the post-spinel reaction - and that other reactions and potentially compositional variations were important in controlling the depth of the seismic discontinuity. Ritsema et al. (2009) used the differential travel-times of S410S and S660S phases (i.e. a proxy for MTZ thickness) to constrain the mantle potential temperature in the North Pacific ($1650 \pm 100\ \mathrm{K}$). Waszek et al. (2021b) inverted SdS data separately for 410 and 660 topographies and then used the calculated MTZ thicknesses to invert for an average potential temperature of 1630 K with a peak-to-peak amplitude of $\sim 350\mathrm{K}$. All of these inversions assume a single global mineral physics model - usually a mechanically mixed (MM) pyrolite model with $f_{bas} \sim 0.2$. The effect of lateral composition variations has only recently been considered. Tauzin et al. (2022) inverted reflection amplitude and transition zone thickness for composition as well as potential temperature, finding that the basalt fraction (f_{Bas}) varied from 0.0 to 0.8 in the mid mantle, finding a similar mantle potential temperature to Waszek et al. (2021b) but a slightly higher peak-to-peak amplitude of ~ 450 K.

The MTZ is dynamically complex - and discontinuity topographies could represent a useful constraint on geodynamic models in the mid-mantle. Papanagnou et al. (2023) outlined a method for predicting seismic discontinuity topography using the thermal structure of a geodynamic model, and examined the effect of using diverse mineral physics tables on the predicted topographies - which had a large effect when applied globally. Many geodynamic codes are now able to produce thermo-chemical outputs (e.g. TERRA (Stegman, 2003), ASPECT (Kronbichler

Symbol	Parameter	Value	
k	Thermal Conductivity	$4\ \mathrm{W m^{-1}\,K^{-1}}$	a
C_P	Specific Heat Capacity	$1100\ \mathrm{J\,kg^{-1}\,K^{-1}}$	b
T_{Surf}	Surface Temperature	300 K	
T_{CMB}	CMB Temperature (average over run)	4007 K	c
γ_{410}	$\frac{dP}{dT}$ of $Ol \rightarrow Wd$	$+1.5\ \mathrm{MPa\,K^{-1}}$	
γ_{660}	$\frac{dP}{dT}$ of $Rw \rightarrow Brm + Pc$	$-1\ \mathrm{MPa\,K^{-1}}$	
η_0	Reference Viscosity	$4 \times 10^{21}\ \mathrm{Pa\,s}$	
E_A	Activation Energy	1.75	
B	Basalt buoyancy number	0.66	
$\frac{\Delta\rho_{410}}{\rho_{410}}$	$Ol \rightarrow Wd$ density change	6.37 %	
$\frac{\Delta\rho_{660}}{\rho_{660}}$	$Rw \rightarrow Brm + Pc$ density change	9.08 %	

Initial Condition: The mantle circulation model is initialised from a mantle convection model run for 2 Gyr. The mantle is preconditioned for 200 Myr using the first stage of the plate model.

[a] (p. 122, Clauser & Huenges, 1995)

[b] (Panton, 2020)

[c] cooling CMB condition, see main text.

Table 1. Parameters used in mantle circulation model 'm_cc_066_u'

et al., 2012; Heister et al., 2017), stag3D (Tackley & Xie, 2002)) - including those generated by geological processes (such as melting (e.g. Van Heck et al., 2016)) and then dispersed through the silicate Earth over Earth history.

Here we present a new method for predicting discontinuity topography in thermochemical mantle circulation models. Further, a seismologically-motivated comparison to global observations is illustrated.

2 METHODS

2.1 Geodynamic model

We demonstrate our method using a single mantle circulation model 'm_cc_066_u' - detailed at length in Davies et al. (2025). This model was run in TERRA (Baumgardner, 1983), which solves the Stokes equations on an iscosahedral grid refined to give a grid spacing of $\sim$ 45km in the mid-mantle. Model parameters are summarised in Table 1. The upper boundary is driven using the plate motion model of Müller et al. (2022). Radial average viscosity structure is illustrated in Figure S1. 'm_cc_066_u' was run using a cooling core mantle boundary (CMB) thermal boundary condition (Davies, 2015), and is internally heated according to concentration of heat producing elements distributed on particles (see below) in the simulated mantle (Panton et al., 2022), and is compressible with a Murnaghan equation of state (Bunge et al., 1997). The radial viscosity structure features a ~ 100 km thick lithosphere that is $100\times$ more viscous than the upper mantle, allowing thermal conduction to dominate there. Therefore this model has most of the thermal physics that we would expect in the convecting silicate Earth, motivating a comparison to seismic observables sensitive to the detail of thermochemical structure. The thermochemical structure at 410 and 660km depth in simulation m_cc_066_u is illustrated in Figure S2.

2.1.1 Composition in TERRA

For full details of the implementation of particles and melting in TERRA, the reader is referred to Stegman (2003), Van Heck et al. (2016), and Panton et al. (2022). TERRA advects particles through its simulations according to the flow calculated on the regular icosohedral grid nodes. These particles can be used as passive tracers, but here have an active effect on the flow due to density anomalies dependent on their bulk composition. In m_cc_066_u, basalt is 5% less dense than lherzolite between 660 and 740km depth. This results in a slight 'basalt density filter' effect where basaltic material is more buoyant than pyrolitic material in the lower-mid-mantle, but the resulting radial basalt segregation is not as extreme as that advocated for by Yan et al. (2020) or that Tauzin et al. (2022) suggest by inversion of global SS precursor structure. Elsewhere, basalt is denser than pyrolite or harzburgite.

Bulk composition is described using a parameter (C) that varies between 0 and 1 describing the relative depletion or enrichment of the particle - a C-value of 0 represents entirely depleted material (i.e. Harzburgite (Hzb)), of 0.2 represents bulk mantle material (i.e. Lherzolite (Lhz)), and of 1 represents entirely enriched material (i.e. Basalt (Bas)/Pyroxenite). Particles are initialised with an even distribution throughout the whole mantle with half of all particles being lherzolitic,

Table 2. Assumed molar composition for our three characteristic lithologies; harzburgite, lherzolite and basalt.

	Harzburgite (Hzb)	**Lherzolite** (Lhz)	**Basalt** (Bas)
SiO_2	36.184	38.819	52.298
MgO	56.559	49.894	15.812
FeO	5.954	6.145	7.121
CaO	0.889	2.874	13.027
Al_2O_3	0.492	1.963	9.489
Na_2O	0.001	0.367	2.244

40% harzburgitic and 10% basaltic - resulting in an initial average C-Value of 0.2. The particles are then advected through the simulation, following the whole-mantle circulation. If the pressure-temperature conditions of the particle put it over the solidus in the shallow mantle, it undergoes partial melting - melt is extracted towards the surface resulting in particles near the surface becoming enriched (basaltic) while the melt source particle become depleted (harzburgitic). As well as bulk composition, various geochemical parameters (e.g. Panton et al., 2022) including abundances of heat producing elements evolving with melt and radioactive decay are recorded on the particles but are not of interest here.

2.2 Mineral physics models

In order to predict the discontinuity topography, we require look-up tables of density (ρ), P-wave velocity (V_P) and S-wave velocity (V_S) in pressure-temperature space for each of our assumed end-member compositions. We describe our end member lithologies by using six oxide components (see Table 2) - chosen to fit published datasets for Harzburgite, Lherzolite and Basalt (Baker & Beckett, 1999; Walter, 2003; White & Klein, 2014, respectively).

Equilibrium mineral assemblages (with resultant elastic and thermodynamic properties) are calculated by Gibbs free energy minimisation using Perple_X (Connolly, 2009), with thermodynamic data from Stixrude & Lithgow-Bertelloni (2005, 2011, 2022) The isotropic elastic seismic velocities are corrected for anelasticity using the model 'Q7g' (Goes et al., 2004; Maguire et al.,

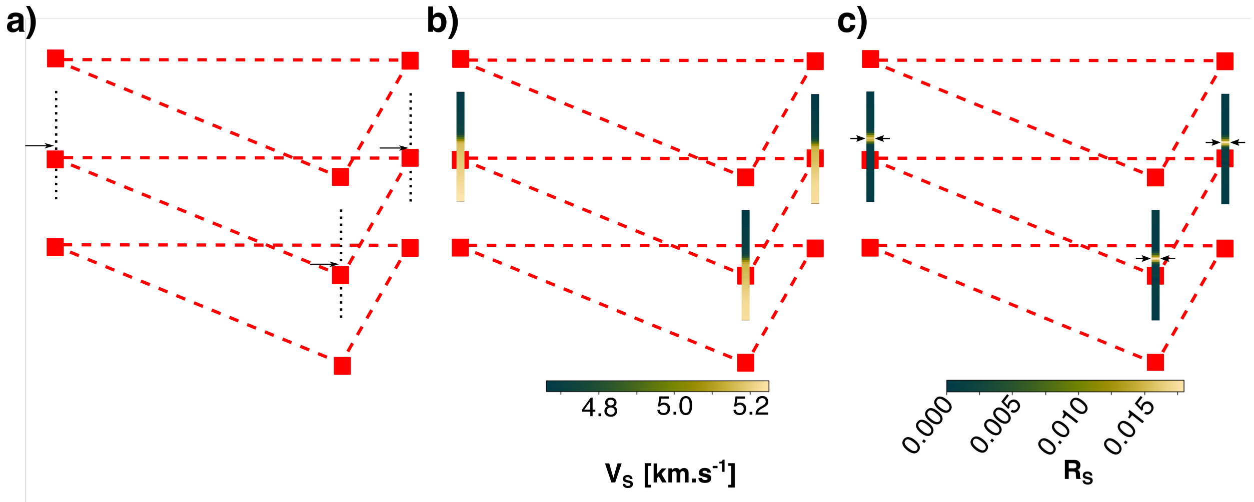

Figure 1. Sketch of method introduced here. *a)* The gridding used for the geodynamic modelling is too coarse for the purposes of finding the discontinuity structure, so the thermal and chemical structures are interpolated onto a finer grid centred on a reference depth (i.e. 410 or 660 km). *b)* temperature, pressure and composition at each interpolated location is used to compute V_S, V_P and ρ. *c)* These are then used to compute S-wave reflectivity R_S at each interpolated location, and the highest reflectivity is used as the discontinuity depth at that location.

2016). The V_S structure of the lherzolite, harzburgite basalt and pyrolitic assemblage (MM18) are shown in Figure S3.

2.3 Prediction of seismic velocity discontinuity ('local mechanical mixing & reflectivity')

Whilst composition is tracked on the fine scale-length of the particles, the total proportion of harzburgite, lherzolite and basalt in the region surrounding each node is also recorded. This then allows us to predict the thermochemcial discontinuity topography on the regular TERRA grid at a spacing of $\sim$ 45km laterally in the mid-mantle, far finer than the the thermochemical structure that SS precursors are sensitive to given that the lateral extent of the first Fresnel zone of S660S and S410S are both ~ 1000 km (Guo & Zhou, 2020), and the full Fresnel zones have sensitivity that extend for several times as far dependent on the azimuth to the source-receiver pair and bands of positive- and negative-sensitivity extending away from the ray-theoretical bouncepoint.

Vertically, however, a 45km vertical resolution is far too coarse to resolve the phase transition, so we first interpolate the data from the coarse TERRA grid onto a finer vertical grid centred on a target depth (for this work 410km and 660km) for each horizontal position (see Figure 1 a). The thermal field of our geodynamic model is smooth, so we interpolate temperature linearly (similar to the method used by Papanagnou et al., 2023) between the TERRA grid-points and since chemical diffusion is very slow composition is interpolated by a nearest neighbour scheme. This allows us to integrate the chemical heterogeneity from the MCM into our discontinuity prediction. Given recent geodynamic and seismologic work (e.g. Yan et al., 2020; Goes et al., 2022) chemical heterogeneity is expected to be quite high in the Earth's mantle.

A mechanical mixing calculation is performed between the tracked compositions at each point to evaluate ρ, V_S and V_P on this refined grid; (Figure 1 b). To gain a representative estimate of the bulk properties, a harmonic average is used for densities and velocities

$$\frac{1}{\Psi^{P,T}_{\mathrm{Bulk}}} = \frac{f_{\mathrm{Lhz}}}{\Psi^{P,T}_{\mathrm{Lhz}}} + \frac{f_{\mathrm{Hzb}}}{\Psi^{P,T}_{\mathrm{Hzb}}} + \frac{f_{\mathrm{Bas}}}{\Psi^{P,T}_{\mathrm{Bas}}} \tag{1}$$

Where $\Psi^{P,T}_{m}$ represents either the density or one of the seismic velocities of the material (m) at the relevant pressure (P) and temperature (T). We refer to this calculation, where the fraction of each end-member in the averaging scheme varies according to the local abundance of each end-member, as 'local mechanical mixing' to differentiate it from the assumption of a uniform mechanical mixture globally.

Having produced the high-resolution density and velocity profiles at each node, we predict the topography as observed by SS precursors, assuming vertical incidence. First, the vertical reflectivity is calculated for each depth i as the impedance contrast across that depth,

$$R^i_S = \frac{(\rho^{i+1} + \rho^i)(V_S^{i+1} + V_S^i) - (\rho^{i-1} + \rho^i)(V_S^{i-1} + V_S^i)}{(\rho^{i+1} + \rho^i)(V_S^{i+1} + V_S^i) + (\rho^{i-1} + \rho^i)(V_S^{i-1} + V_S^i)} \tag{2}$$

To then find the discontinuity depth, the peak vertical reflectivity is found at each lateral node, and the corresponding depth used (Figure 1 c) since we assume the peak vertical reflectivity is associated with the depth of the discontinuity. The peak vertical reflectivity represents an upper bound for the actual reflectivity for the offsets used in SS precursor studies since the SS-precursor phase is not strictly vertically incident on the discontinuity. Whilst for 410, this is usually unambiguous as across compositions it is generally controlled by the Ol-out reaction (until the pyroxene-garnet reaction dominates at high basalt fraction), the region around 660 is much more complex. At cool temperatures the spinel-out reaction is accomplished via akimotoite (e.g. Yu et al., 2011; Cottaar & Deuss, 2016) and at high basalt fraction the spinel out reaction is replaced by the deeper garnet-out reaction (e.g. Jenkins et al., 2016) - together these can result in multiple peaks and broad regions of elevated reflectivity (see figure S4). For simplicity we pick the depth of maximum reflectivity.

2.4 The 'bouncepoint-spherical cap filter' – a simple filter for SS precursors

Later, we will compare these predicted topographies to those observed using SS-precursors, and here describe a simple filter to permit a meaningful comparison.

As the distribution of sources, receivers, and therefore bounce-points, are highly non-uniform and SS-precursor sensitivity extends away from the ray-theoretical bounce-point (e.g. Neele et al., 1997; Dahlen, 2005; Guo & Zhou, 2020) we implement here a first-order approximation of the sensitivity of the precursors to mid-mantle seismic structure distributed with the ray-theoretical bounce-points. We approximate the sensitivity of the precursor (typically of period ~ 20 s), which is actually a complex region of positive and negative traveltime sensitivity, as a spherical cap of radius 500 km. This spherical cap represents a multi-azimuthal average of *SS-SdS* traveltime sensitivity and is similar in size to the first Fresnel zone of the SS precursor(e.g. Dahlen, 2005). Similar caps are typically used in stacking these SS precursor data (e.g. Houser et al., 2008; Guo & Zhou, 2020). As well as this finite-far-field sensitivity seismic waves cannot resolve infinitely thin radial seismic impedance structures. Usually it is assumed that impedance contrasts less than a quarter wavelength thick cannot be resolved (e.g. Chambers et al., 2005).

This 'filter' is very simple and does not capture all of the complexities of the physics of seismic ray reflection. In regions with many bounce-points and a reasonable spread of azimuths (e.g. the North Pacific) use of the true sensitivity kernels is unlikely to have a significant impact on the expected topography. However, in poorly constrained regions we likely under-predict the high spherical harmonic degree structure compared to that retrieved by a realistic kernel. We also do not consider the effect of earthquake focal mechanisms (which would create a null-sensitivity along the nodal planes (Zhao & Chevrot, 2003)) or anisotropic velocities in the mid-upper mantle

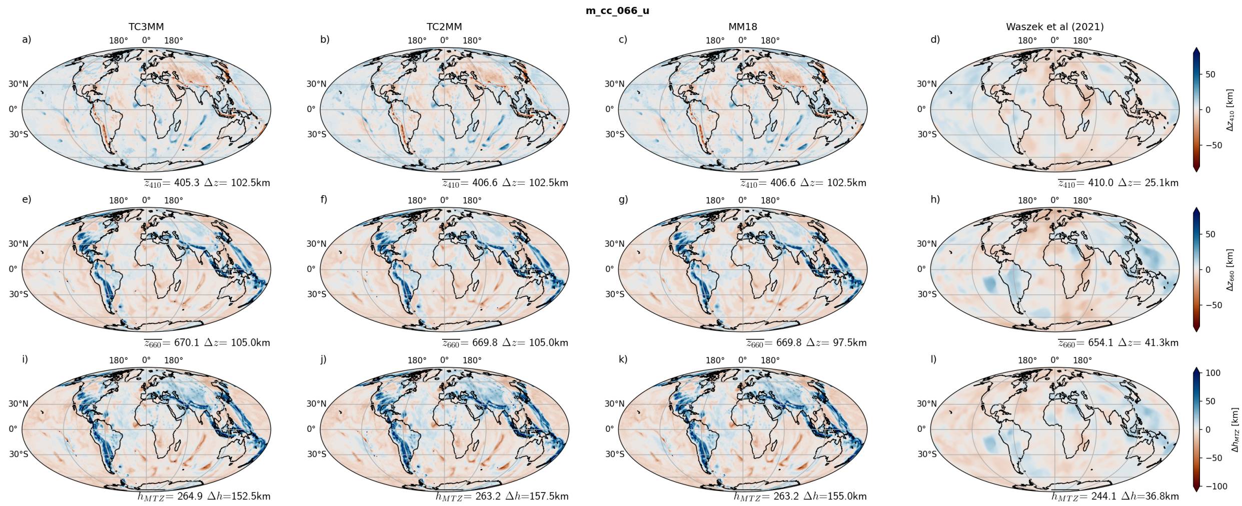

Figure 2. Topography on 410 (*a-d*) and 660 (*e-h*) discontinuities and MTZ thickness variations (*i-l*) calculated by method described here for model 'm_cc_066_u' compared to the topography found for the Earth by Waszek et al. (2021b) in the righthand most column (*d, h, l*). The other columns denote different methods of mechanical mixture. *'TC3MM'*: topography predicted by three end-member local mechanical mixing calculation using a equilibrium assemblage table for Lhz. *'TC2MM'*: topography predicted by two end-member local mechanical mixing calculation using a Mechanical Mixture table of 80% Hzb, 20% Bas for Lhz. *'MM18'*: topography predicted by a global mechanical mixing calculation of 18% Bas and 82% Hzb.

(Huang et al., 2019) since we judge these to have a secondary impact on recovered topographies compared to the above.

To produce the filtered topographies, we do the same upscaling and local mechanical mixing procedure described above, but instead of focusing on the region around the discontinuities, we predict the fine-scale material property structure on the length scale of the thermodynamic tables ($2.5\mathrm{km}$) radially throughout the MTZ. For a $20\mathrm{s}$ period SS precursor just beneath d660, a quarter wavelength is $30\mathrm{km}$, so we use a rolling window $30\mathrm{km}$ thick to find the radial reflectivity structure through the whole MTZ at each lateral point. We then pick the depths with the brightest reflection around $410\mathrm{km}$ ($200-480$ km) and $660\mathrm{km}$ ($600-850$ km depth) depth as the depths of the discontinuities. To filter the predicted topographies for the lateral sensitivity of the SS precursor, we take a simple average of the discontinuity depth within a radius of 500 km of the bounce-points for the source-receiver pairs used by Waszek et al. (2021b).

3 RESULTS

3.1 Local mechanical mixing with three endmembers: TC3MM

First we consider the topographies calculated with three end members, referring to this local mechanical mixing model as 'TC3MM' (since this takes account of the full thermochemical structure with three-endmembers). The global discontinuity topography predicted by this method is illustrated in Figure 2 a, e & i. The topography on these reactions is dominated by the focused upwellings (approximating plumes) and downwellings (approximating slabs) that pass through the MTZ of the model - but there are other regions of complex topography particularly on d410 above flat-lying slabs such as beneath Eastern Canada and NE Brazil. On d410, as suggested by the classic understanding that the discontinuity is controlled by the Ol-out reaction with a positive Clapeyron slope, hot upwellings are associated with a deepening of the discontinuity and cool downwellings are associated with an elevation.

On d660, the broad-scale structure follows the trends expected if we assume the topography is dominantly controlled by the Ringwoodite-out reaction, which has a negative Clapeyron slope (i.e. that the downwellings have a deeper associated discontinuity and the upwellings have a shallower discontinuity). The much wider spatial extent of the topography associated with downwellings on d660 compared to d410 (e.g. Western Pacific) is noticeable. This is explained by the greater viscosity around d660 than d410 in the geodynamic model (the viscosity in the geodynamic model starts to increase in the lower part of the mantle transition zone, so is already elevated compared to around d410 see figure S1).

3.2 Effect of local mechanical mixing on discontinuity topography

One of the distinctive aspects of the method presented here compared to previous work (Papanagnou et al., 2023) is that we consider the effect of lateral variations of composition on discontinuity topography. We can also predict the topography by the same peak R_S method, but by assuming a fixed (mechanically mixed) composition or by assuming instead that lherzolite represents a mechanical mixture of harzburgite and basalt get a sense of the effect the local mechanical mixing and the number of endmembers has on the topography. The effects are small, but these simpler

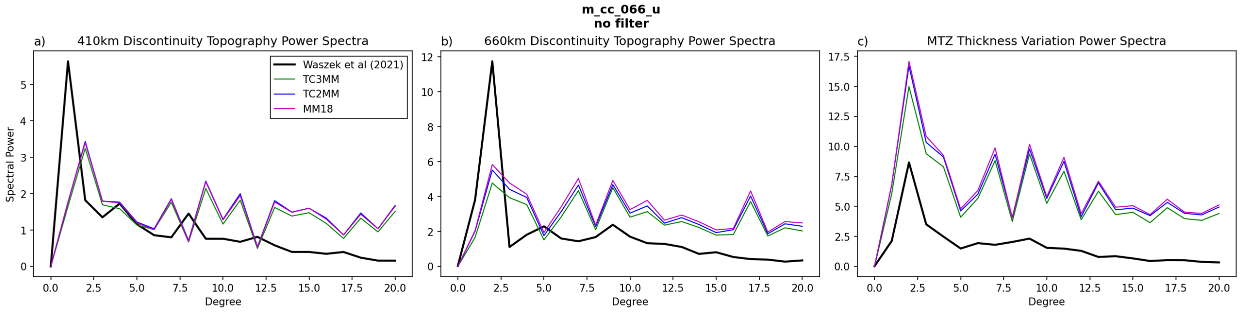

Figure 3. Power spectra of *a)* 410 discontinuity topography, *b)* 660 discontinuity topography, *c)* MTZ thickness variations for predicted seismic structures with different mechanical mixing methods, as discussed in text, TC3MM – local mechanical mixing with three endmembers, TC2MM – local mechanical mxing with two endmembers, MM18 – global mechanical mixture. Power spectra of topography calculated by Waszek et al. (2021b) are included for reference.

chemical assumptions have more power in the spherical harmonic spectra than TC3MM at most spherical harmonic degrees (Figure 3).

3.2.1 Reducing the number of endmembers to two: TC2MM

We track composition in TERRA on three end members (see above). This implicitly assumes that the entire mantle has not been completely processed since Earth's solidification, and that at the start of our model evolution (1.2 Gyr before present), a large part of it was un-processed. We can change this assumption by replacing the Lherzolite tables (representing a pyrolitic equilibrium assemblage) of seismic properties with a mechanical mixture of basalt and harzburgite, corresponding to $f_{Bas} = 0.2$ – representing the same bulk composition but as a mixture of the two end members. We refer to this local mechanical mixing model as 'TC2MM' (since we have reduced our consideration of the thermochemical structure to a consideration of two endmembers). The resulting discontinuity topographies are shown in figure 2 b, f, & j – with no significant differences in the distribution of topographic anomalies. On d410, the topographic anomalies in Figure 2 b are generally shifted to deeper values, with a deepening of the average discontinuity depth globally. On d660 (Figure 2 f), the average discontinuity depth becomes shallower (but only by 300m).

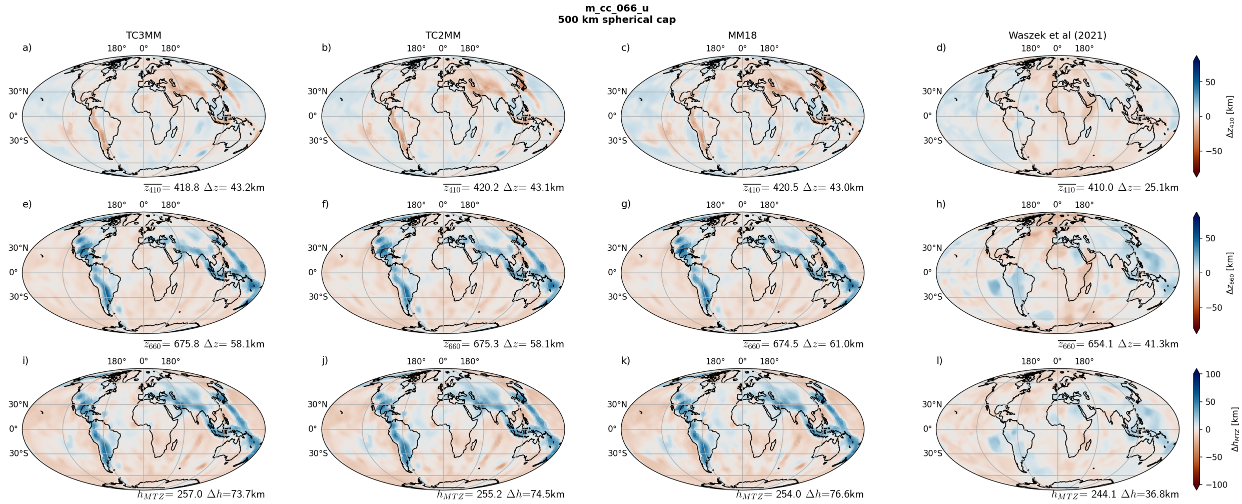

Figure 4. Topography on 410 (*a-c*) and 660 (*e-g*) discontinuities and MTZ thickness variations (*i-k*) calculated by the method described here, then filtered using a 500 km spherical-cap-bouncepoint method, compared to the topography on 410 and 660 and MTZ thickness variations described by Waszek et al. (2021b) in *d*, *h* and *l* respectively.

3.2.2 Uniform global mechanical mixture: MM18

Similarly to the section above, we can form a table representing a global mechanical mixture by mixing our end-member tables of Lhz, Hzb and Bas. A commonly assumed global mantle composition is a pyrolite model - a mechanical mixture of $\sim 20\%$ basalt and $\sim 80\%$ harzbugite - following previous work (Papanagnou et al., 2023; Ritsema et al., 2009), we use a value of $f_{Bas} = 0.18$ (the 'MM18' pyrolite model) for this comparison. The resulting calculated topography is shown in Figure 2 c, g, & k. As this global mechanical mixture has only two end-members a comparison is best made with the local mechanical mixture TC2MM. The average discontinuity depths are similar between the two models, and very few differences can be seen on d410 or d660.

3.3 Effect of bouncepoint-spherical cap filter on recovered discontinuity topographies

So far, we have only calculated the geographic distribution of peak reflectivity depth and have not considered how this is observed seismically. Above (section 2.4), we described a simple filter that captures some of the key physics, and we consider the effect of that filtering on recovered topographies here.

The topographies of d410 and d660 calculated from the MCM shown in Figure 2 are filtered by

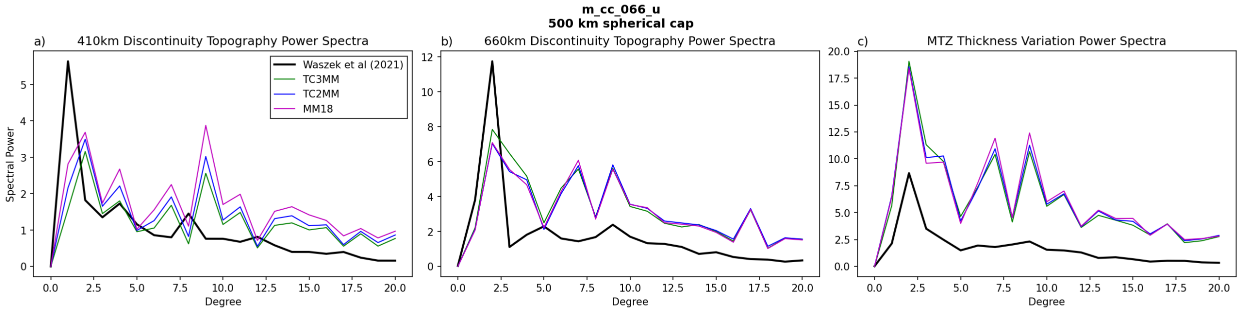

Figure 5. Power spectra of *a)* 410 discontinuity topography, *b)* 660 discontinuity topography, *c)* MTZ thickness variations for filtered predicted seismic structures with different mechanical mixing methods, as discussed in text, TC3MM – local mechanical mixing with three endmembers, TC2MM – local mechanical mixing with two endmembers, MM18 – global mechanical mixture. Power spectra of topography calculated by Waszek et al. (2021b) are included for reference.

this method and shown in Figure 4. Note the significant reduction in the peak-to-peak amplitude of topography, and how the focused elevation of topography on the d410 beneath subduction zones in the unfiltered predicted topography is broadened to a similar width as that seen in the observed topography of d660. Fine-scale features such as the lateral offset of d410 and d660 due to steps in the surface motion patterns (e.g. beneath the Hindu-Kush) are lost. Power spectra for the filtered predicted topographies are plotted in Figure 5. For d660 and MTZ thickness variations, filtering reduces the difference between the topographies predicted with different mixing methods (compare Figures 3 and 5), although on d410 there appears to be increased sensitivity to the filtering method. Irrespective of the mixing method, at high spherical harmonic degree the power on d410, d660 and MTZ thickness variation is significantly reduced when the 'filtering' is applied. Whilst the bouncepoint-spherical-cap filtering improves the match between the predicted topographies and the topography reported by Waszek et al. (2021b) (compare the coloured lines to the black line in Figures 3 and 5) at high spherical harmonic degrees ($l > 7$), it does not significantly reduce the spectral power at medium spherical harmonic degree ($3 < l < 7$) or increase it at low spherical harmonic degree ($l < 3$), where there is a particularly strong mis-match between the predicted unfiltered power spectra and the seismologically observed topography structure.

We illustrate the effect of varying the spherical cap radius in Figure S7. Even with a comparatively small cap radius (250 km), the predicted topography is considerably smoothed (Figure S7 a & b). With a larger cap than that which we use here in the main text (1000 km radius), topography structure is further smoothed and the peak-to-peak amplitude is slightly underpredicted, and the power on high spherical harmonic degrees ($l > 7$) topography amplitude is under-predicted (Figure S7 g & h).

Considering the variations in MTZ thickness (Figure S7i), there is an overprediction of power at all spherical harmonic degrees for spherical caps smaller than 1000 km, and for a cap of radius 1000 km a good fit is only observed at high spherical harmonic degree ($l > 12$), where structure on d410 and d660 is completely smoothed by the cap. On d410 and d660 this largest cap predicts a spectra that matches the Waszek et al. (2021b) spectra from $l \sim 3$ out to $l = 20$. This suggests that the lengthscales of the topographies on d10 and d660 are individually reasonably correct for this large cap, but that they result in an excessively rough transition zone thickness structure – i.e. that they are excessively anti-correlated for this combination of MCM and mineral physics tables.

We additionally illustrate the effect of filtering regionally in Figure S6. Small-scale downwellings around 410 km depth, which produced narrow ridges on d410 are washed out in the filtered topography. Complex topography within the downwellings on d660 is lost, as well as the slight shallowing of the discontinuity beneath Florida and the Eastern Gulf of Mexico.

3.3.1 Predicted dip of discontinuity surfaces

Related to the short length-scales of the unfiltered topography, the resulting topography has some slope everywhere but apart from in downwellings and immediately around upwellings is reasonably smooth, with slopes of less than 45°. However, the discontinuity surface is predicted to be significantly steeper (around $70°$ slope) around downwellings (See Figure 6). On filtering, whilst the recovered topography is smoother, sub-vertical regions around upwellings and downwellings remain. The seismological significance of this will be discussed in section 4.1.2.

3.3.2 Lateral variations in reflectivity of predicted discontinuity structures

The relative amplitude of SS precursors to the main SS arrival is also of interest since it has been used to invert for the basalt fraction in the mid-mantle (Tauzin et al., 2022), and we have taken

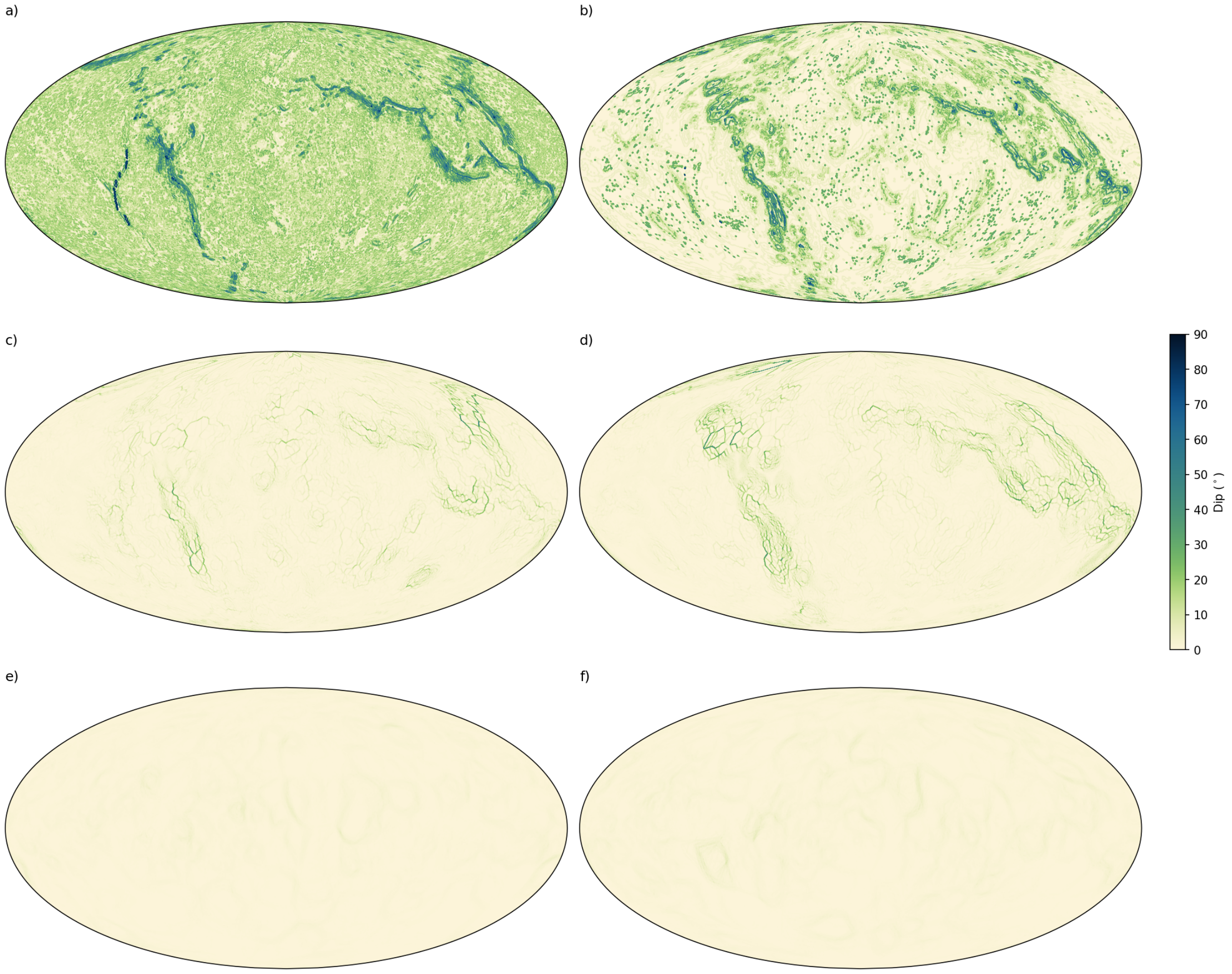

Figure 6. Dip of surface of (*a*, *c*, & *e*) d410 and (*b*, *d*, & *f*) d660 for unfiltered predicted topography (TC3MM) (*a* & *b*), filtered (500 km radius bouncepoint spherical cap) predicted topography (*c* & *d*), Waszek et al. (2021b) topography model (*e* & *f*)

the discontinuity reflectivity as a proxy for this amplitude ratio – see discussion in section 4.1.3. We plot the lateral distribution of peak R_S^{410} and R_S^{660} in Figure 7. The mismatch between the geographic distribution of high R_S^d regions predicted by this simulation and areas with high SS precursor amplitudes is strong. Local mechanical mixing is more important in local variations in R_S^d structure than for the discontinuity topography, with the 'bright' spots around upwellings less intense, and more short-wavelength structure noticeable (Figure S8) than in the reflectivity structure predicted from a global mechanical mixture. The variations we find here in d660 reflectivity due to variations in the thermal structure of the MCM are of a similar magnitude to those interpreted to be due to chemical variations within the mantle, but have a different geometry – being aligned

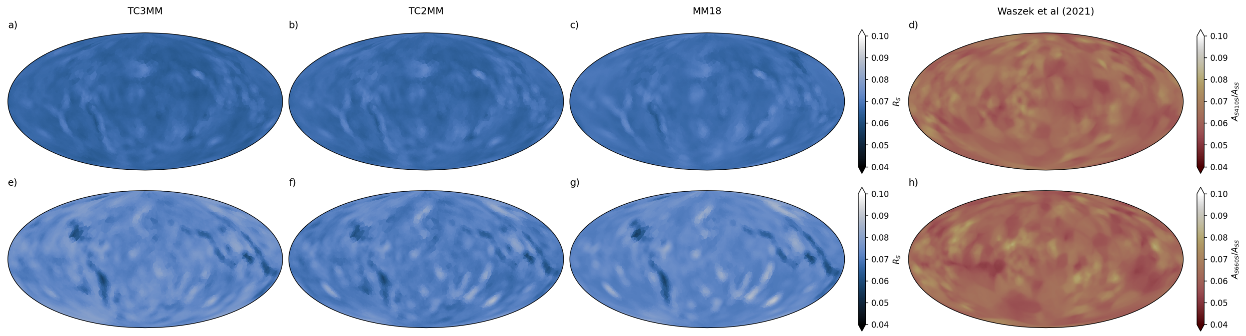

Figure 7. R_S (Shear wave reflectivity) on d410 (*a–c*) and d660 (*e–g*) for each of the mechanical mixing methods considered in this paper TC3MM (*a* & *e*), TC2MM (*b* & *f*), and MM18 (*c* & *g*) are compared qualitatively to the amplitude of the SS precursor (*d* and *h*), filtered using the bouncepoint spherical cap of radius 500 km (and 'thickness' of 30km. Note the poor fit in geographic distribution between the geodynamic predictions and the data of Waszek et al. (2021b). The average reflectivities of d410 and d660 are more different (e.g. for TC3MM 0.066 and 0.073 respectively) than the average normalised amplitude of the precursors in the Waszek et al. dataset (0.038 and 0.037 respectively).

along downwelling and upwelling centres, unlike in the Waszek et al. (2021b) dataset where high amplitude regions are not obviously associated with the location of slabs or large plumes in the Earth. The variations in the reflectivity of d410 are smaller than on d660, but again are closely associated with the distribution of downwellings and upwellings in the MCM. We expand on the significance of the reflectivity variations in section 4.1.3

4 DISCUSSION

Given the desire to better understand mantle circulation from the discontinuity topographies, we now compare the set of predicted topography from the mantle circulation model with those observed on the real Earth.

4.1 Comparison to SdS-derived topography

For global geodynamic simulations, the natural point of comparison are global SS-precursor topographies (e.g. Waszek et al., 2021b; Guo & Zhou, 2020; Houser, 2016). As an example we here make a comparison to the topography model of Waszek et al. (2021b), derived from SS precursors in seismograms filtered for a period of $15 - 50$ s. A naive comparison between our calculated topographies in the geographic (Figure 2) and spectral domains (Figure 3) is not encouraging – our peak-to-peak topography is much larger (~ 100 km on d410 and d660) than that found by Waszek et al. (2021b) (~ 28 km and ~ 45 km respectively), and our structure is focused on short-wavelengths (high spherical harmonic degree) particularly around downwellings.

4.1.1 Mid mantle temperature ranges larger than those inverted from SS precursors consistent with SS precursor derived topography structure.

The topography that we naively predicted from a mantle circulation with a mid-mantle temperature range of ~ 2000 K that drives vigorous convection compared poorly to the topography recovered from SS-precursors (~ 100 km on each of d410 and d660, 150 km on the transition zone thickness variations compared to ~ 40 km observed on all three in recent studies (e.g. Houser, 2016; Guo & Zhou, 2020; Waszek et al., 2021b)). However, when a seismologically-motivated cap of radius 500 km is applied, the topographies become directly comparable to those inverted by Waszek et al. (2021b) and Tauzin et al. (2022) to a much smaller temperature range of 400 K. Of course, this is dependent on the cap size, and many models in principle could be over-smoothed until they are compatible with observations, but given the contribution to total sensitivity away from the first Fresnel zone is small with increasing radius (e.g., Guo & Zhou, 2020, figure 4) doing this would not be seismologically motivated. We note that the range of depths for d410 and d660 when filtered with the largest cap in figure S7 are within a couple of kilometres of the ranges for d410 and d660 reported by Waszek et al. (2021b).

4.1.2 Predicted discontinuity topography extremely steep around downwellings

We highlighted the steep dips on the d410 and d660 predicted topography surfaces (see section 3.3.1). Here we sketch some seismologic implications. Such a steep discontinuity topography structure could significantly complicate the physics of reflection, potentially changing the location of bounce-points away from the mid-point of the source-receiver great circle (e.g. Rochira & Thomas, 2023) and significantly changing the reflectivity-offset curve. Whilst the global topographies inverted in SS-precursor studies, such as the Waszek et al. (2021b) model we compare to here, are smooth and rolling (dips not exceeding $15°$) there is some evidence that the discontinuity surface in the Earth could be considerably rougher, at least in places. Rochira & Thomas (2023) showed that some SS- and PP-precursors that could be interpreted as reflectors in the deeper mid-mantle (e.g. Waszek et al., 2018) were, when the back-azimuth was taken into account in the bounce-point location, more accurately located around d410 and d660. Whilst these out-of-plane reflections could be due to compositional or thermal structure associated with the downwelling in the study region, SdS reflected out of the great-circle plane is also a possibility (Rochira & Thomas, 2023). Neele et al. (1997); Neele & Regt (1999) considered the topography of a discontinuity around slabs with a similar magnitude to that presented here, showing the smearing of the intense deflection away from the slab regions they were imposed within, also creating effects far from the downwelling slab. However, the deflections in unfiltered discontinuity topography we predict are much steeper than the sinusoidal topographies used by Neele et al., and we expect significant deflections both due to slabs and upwellings. To properly assess the validity of the simple spherical cap filter, we would need to propagate seismic waves through regions of our predicted mid-mantle reflectivity structures to see what structures are recovered, compared to the 'filtered' topographies presented here.

4.1.3 Significance of lateral reflectivity variations in the Earth and predicted discontinuity structures

Tauzin et al. (2022) use the observed variations of MTZ thickness and the amplitude of SS precursors to invert for the thermochemical structure – finding that variations of transition zone thickness (a function of d410 and d660) are largely sensitive to temperature variations only and not chemical variations, although we do find significant variation in our discontinuity reflectivity even for constant composition (see figure 7.

The relative amplitude of the SS precursor phase should be mainly controlled by the reflectivity of the discontinuity, that we used for the prediction of the depth of the discontinuities, but is also controlled by any attenuation along the ray-path, which is not trivial to assess. For now, we accept R_s^d as a proxy for A_{SdS}/A_{SS}, but note these potential sources of error. Interrogating our tables we produce a similar relationship between MTZ thickness and R_S for varying f_{Bas} and T as found by Tauzin et al. (2022) (Figure S10) – which suggests that using R_S^{410} or R_S^{660} as an initial proxy for SS precursor amplitudes is not unreasonable.

The average reflection amplitude of S410S and S660S is similar in the Waszek et al. (2021b) dataset (d410 is 2.5% brighter than d660), but in the discontinuity structure predicted from this simulation, d660 is significantly (10%) brighter than d410, using the three-end-member mechanical mixing (TC3MM, figure 7). Varying the fraction of basalt in a global mechanical mixture (Figure S8) allows $R_S^{660} \sim R_S^{410}$ where $f_{\mathrm{Bas}}^{660} > f_{\mathrm{Bas}}^{410}$. This geodynamic model doesn't have an accumulation of enriched material in the mid-mantle, but this suggests that a better fit to the Earth may be observed for a geodynamic simulation with basalt enrichment in the basalt density filter (e.g. Davies, 2008; Yan et al., 2020).

Plotting histograms of SdS amplitude from the Waszek et al. (2021b) model and values of R_S^d predicted for this geodynamic model (Figure S11), we highlight how the reflectivity is much less variable for the predicted discontinuities than the observed precursor amplitudes. This could suggest that this geodynamic simulation underestimates the compositional variability in the mid-mantle, particularly given the range of reflectivity predicted for the various global mechanical mixtures (see figure S12). Other factors, such as the roughness of the discontinuity surface may also play an important role (see above).

4.2 Relative importance of thermal and compositional heterogeneity for discontinuity topography

When considering the predicted topographies by this method (figure 2) for a MCM with moderate compositional variations we find that the local mechanical mixing has essentially no effect, particularly once filtered for what is seismically visible (figure 4). We do show some subtle differences in the reflectivity structure for discontinuities picked from different mixing assumptions (figure 7), but in the model we have shown here there is not a drastic difference for the different assumptions about composition mixing.

If we vary the composition of the whole mantle according to different proportions of basalt and 'pyrolite' in a global mechanical mixture in the range of $0.1 < f_{bas} < 0.5$ we see no significant change in predicted filtered topographies (see figure S9), highlighting that for moderate changes in mantle composition, any changes are limited to changes in lateral reflectivity structure.

This highlights that for reasonable mantle transition zone compositions, d410 and d660 topographies are explained principally by the decomposition of Ol and Rw, and that the reflectivity is affected by the relative abundance of enriched basaltic material.

4.3 Is MTZ discontinuity structure a useful constraint on MCMs?

4.3.1 Topography of d410 and d660

Fitting the observed topographies of d410 and d660 in the Earth from a MCM is a complex combination of thermochemical structure, the correct application of mineral physics tables, and any seismological filtering. We have shown that even a very simple seismology-motivated smoothing filter obscures a lot of the fine detail of topography structure, and have discussed the composition-independence of the topographies of d410 and d660.

The thermal structure of the mid-mantle is dominated by downgoing slabs and upwelling plumes, and is also expected to control the discontinuity structure. The location and morphology of the downgoing slabs are largely a function of the surface motion history, which in MCMs is imposed at the surface. However, the remainder of the thermal structure is a function of the reaction of the convecting mantle to the imposed downwellings and does vary between geodynamic models with different dynamic structures. The geodynamic significance of interpretations of the topographies of individual discontinuities is disputed, due to the potential dominance of uncorrected upper mantle velocity structure in the differential travel-times of the SS and SdS phases (e.g., Tauzin et al., 2022). This makes it challenging to interpret poorly fitting (geographically or spectrally) predicted individual topographies in terms of geodynamics.

4.3.2 Variations in MTZ thickness

As the transition zone thickness is determined by the differential travel times of S660S and S410S, without reference to the SS phase, it should not be sensitive to upper mantle velocity structure variations (e.g. Tauzin et al., 2022). Sadly this approach limits the ability to consider separately the thermal structure at 410 and 660km depth, although generally the offset in convective thermal structures between 410 and 660 km depth is generally expected to be small compared to the 1000 km width of the SS precursors' first Fresnel zone. This potentially suggests that variations of transition zone thickness can give a sense of the fit between the simulated and true Earth's lateral thermal structure at the scalelengths SS precursors are sensitive to. At longer periods than the SS-precursors that are used for calculations of d410 and d660 topography Koroni et al. (2017) showed that S410S had significant sensitivity at 670 km depth, potentially suggesting that S410S-S660S might not be a simple proxy for MTZ thickness. We do not consider this further here, but note that it is still worth considering d410 and particularly d660 individually in addition to the transtion zone thickness.

4.3.3 Reflection amplitude structure

Fit to reflection amplitude structure is more complex – as reflection amplitude structure has a strong compositional component, it is sensitive to the longterm evolution and residence of melt-derived heterogeneity in the lower mid-mantle (Tauzin et al., 2022). The amount and distribution of basaltic material at the base of the MTZ should be a function of the history of melt-production, history of convection, the relative behaviours of enriched and depleted material in the MTZ, other heterogeneities in the mantle, as well as the uncertainties in mineral physics and seismological filtering of the mid-mantle. However, even in a well mixed mantle such as that produced by this MCM, lateral variations in R_S^d exist, largely driven by thermal structure instead of compositional variations. This suggests that fit to reflection amplitude structure may emerge from a well-fitting model but may not be a useful metric in searching for one.

4.3.4 Characteristics of an Earth-like MCM

An Earth-like MCM, when filtered for the sensitivity of SS precursors should match the predicted depths of d410 and d660, and the amplitude of the discontinuity topographies and transition zone thickness should match that observed. The spherical harmonic spectra of the predicted discontinuities should peak on degree 1 or 2 and then decay approximately monotonically with increasing spherical harmonic degree. These reflect the correct thermal structure globally (average discontinuity depths) and the correct lateral variations of temperature (discontinuity topographies). From the predicted reflectivity structure the global distribution of 'bright' and 'dark' spots should match the reported amplitude structure, indicating a reasonable thermochemical structure. However, we anticipate this as a challenging metric to match since the amplitude of reflected waves is a function of the thermal and chemical structures (the latter of which is sensitive to the history of the delivery of compositional heterogeneity to the mid-mantle), and is possibly more sensitive to the correct 'seismological treatment' than the discontinuity topographies.

4.3.5 Limitations of the candidate model

Whilst we do predict the mean depths of d410 and d660 well, we over predict the topography on both discontinuities (by a factor of about 1.7 for d410 and 1.5 for d660). We over predict both the MTZ thickness and range of discontinuity depths, as well as the power of the spectra at all degrees. This suggests a poor match between the thermal structures of our MCM and Earth's. However, there are many regions where the distribution of thick and thin regions of the MTZ is encouraging (see figure 4).

The comparison between the predicted reflectivity structure and the amplitude structure is less straight-forward. We do not consider the reflectivity of the Earth's surface underside. Similar to the effect of shallow structure on travel times, the reflectivity of the Earth's surface could be highly dependent on regions of partial melt, the thickness of lithosphere or crust, the presence of oceans and icecaps and the roughness of surface topography. However, we do not correctly predict the relationship between the mean reflectivity values of d410 and d660, which the Waszek et al. data suggest are similar, but with d410 slightly brighter than d660. We predict d660 as slightly brighter than d410, which might reflect the under prediction of basalt fraction around 660km depth in this simulation.

Whilst this assessment has shown that m_cc_066_u is not an ideal geodynamic model, it highlights the utility of considering the discontinuity topography as we have here, as it has allowed us to take a mantle circulation model that is fairly reasonable (Davies et al., 2025) and critically assess its mid-mantle structure, and potentially informs the parameter space where we might seek a better-fitting model.

5 CONCLUSION

We predict the topogoraphy of d410 and d660 for a thermochemical MCM. The Fresnel Zone of SS precursors has a significant impact on the recovered topography, and when we apply a simple filter to our predicted topographies we can compare the predicted topographies of d410 and d660 to those inverted from SS precursors meaningfully. Lateral chemical variations seem to have a limited role in controlling the topography predicted from a well-mixed thermochemical MCM, although appear important in explaining the discontinuity reflectivity structure.

We assessed a candidate mantle circulation model using its discontinuity topography and reflectivity structure, finding the range of discontinuity depths were too large on both d410 and d660 and that reflectivity structure predicted from this model does not match global observations well. This is interpreted as suggesting a smaller range of temperatures and more recycled heterogeneity in the MTZ than in our geodynamic model considered here.

ACKNOWLEDGMENTS

This work used the ARCHER2 UK National Supercomputing Service (https://www.archer2.ac.uk) for all geodynamic simulations. All maps have been produced using Cartopy (Met Office, 2010). All colourmaps are taken or adapted from (Crameri et al., 2020). All spherical harmonic routines accomplished using pyshtools Wieczorek & Meschede (2018).

DATA AVAILABILITY

The thermochemical field of the mantle circulation model m_cc_066_u is available for download via Zenodo (Davies et al., 2024, available at https://doi.org/10.5281/zenodo.13960492), and similar mineral-physics tables are released there. The topographies were calculated using Python3 codes 'TERRA-tumulus' released publicly here: `https://doi.org/10.5281/zenodo.15630096`. We compared our topographies to the model released by Waszek et al. (2021b) available via the ISC's Seismological Dataset Repository (Waszek et al., 2021a, available at `https://doi.org/10.31905/7M3LMG8X`)).

This paper has been produced using the Blackwell Scientific Publications GJI LaTeX2e class file.

References

Agius, M. R., Rychert, C. A., Harmon, N., Tharimena, S., & Kendall, J. M., 2021. A thin mantle transition zone beneath the equatorial Mid-Atlantic Ridge, *Nature*, **589**(7843), 562–566, doi: 10.1038/s41586-020-03139-x.

Baker, M. B. & Beckett, J. R., 1999. The origin of abyssal peridotites: a reinterpretation of constraints based on primary bulk compositions, *Earth and Planetary Science Letters*, **171**(1), 49–61, doi: 10.1016/S0012-821X(99)00130-2.

Baumgardner, J. R., 1983. *A Three-Dimensional Finite Element Model for Mantle Convection*, University of California, Los Angeles.

Birch, F., 1952. Elasticity and constitution of the Earth's interior, *Journal of Geophysical Research (1896-1977)*, **57**(2), 227–286, doi: 10.1029/JZ057i002p00227.

Bonatto, L., Schlaphorst, D., Silveira, G., Mata, J., Civiero, C., Piromallo, C., & Schimmel, M., 2024. Unveiling the Distinct Structure of the Upper Mantle Beneath the Canary and Madeira Hotspots, as Depicted by the 660, 410, and X Discontinuities, *Journal of Geophysical Research: Solid Earth*, **129**(5), e2023JB028195, doi: 10.1029/2023JB028195.

Bunge, H. P., Richards, M. A., & Baumgardner, J. R., 1997. A sensitivity study of three-dimensional spherical mantle convection at 108 Rayleigh number: Effects of depth-dependent viscosity, heating mode, and an endothermic phase change, *Journal of Geophysical Research: Solid Earth*, **102**(6), 11991–12007, doi: 10.1029/96jb03806.

Burky, A. L., Irving, J. C., & Simons, F. J., 2023. The mantle transition zone beneath eastern North America: Receiver functions and tomographic velocity models, *Physics of the Earth and Planetary Interiors*, **340**, 107035, doi: 10.1016/j.pepi.2023.107035.

Chambers, K., Deuss, A., & Woodhouse, J. H., 2005. Reflectivity of the 410-km discontinuity from PP and SS precursors, *Journal of Geophysical Research: Solid Earth*, **110**(B2), doi: 10.1029/2004JB003345.

Chevrot, S., Vinnik, L., & Montagner, J.-P., 1999. Global-scale analysis of the mantle Pds phases, *Journal of Geophysical Research: Solid Earth*, **104**(B9), 20203–20219, doi: 10.1029/1999JB900087.

Clauser, C. & Huenges, E., 1995. Thermal Conductivity of Rocks and Minerals, in *A Handbook of Physical*

Constants: Rock Physics and Phase Relations, vol. 3 of **AGU Reference Shelf Series**, ed. Ahrens, T. J., American Geophysical Union.

Collier, J. D. & Helffrich, G. R., 2001. The thermal influence of the subducting slab beneath South America from 410 and 660 km discontinuity observations, *Geophysical Journal International*, **147**(2), 319–329, doi: 10.1046/j.1365-246X.2001.00532.x.

Connolly, J. a. D., 2009. The geodynamic equation of state: What and how, *Geochemistry, Geophysics, Geosystems*, **10**(10), doi: 10.1029/2009GC002540.

Cottaar, S. & Deuss, A., 2016. Large-scale mantle discontinuity topography beneath Europe: Signature of akimotoite in subducting slabs, *Journal of Geophysical Research: Solid Earth*, **121**(1), 279–292, doi: 10.1002/2015JB012452.

Crameri, F., Shephard, G. E., & Heron, P. J., 2020. The misuse of colour in science communication, *Nature Communications*, **11**(1), 5444, doi: 10.1038/s41467-020-19160-7.

Dahlen, F. A., 2005. Finite-frequency sensitivity kernels for boundary topography perturbations, *Geophysical Journal International*, **162**(2), 525–540, doi: 10.1111/j.1365-246X.2005.02682.x.

Davies, C. J., 2015. Cooling history of Earth's core with high thermal conductivity, *Physics of the Earth and Planetary Interiors*, **247**, 65–79, doi: 10.1016/j.pepi.2015.03.007.

Davies, G. F., 2008. Episodic layering of the early mantle by the 'basalt barrier' mechanism, *Earth and Planetary Science Letters*, **275**(3-4), 382–392, doi: 10.1016/j.epsl.2008.08.036.

Davies, J. H., Panton, J., Altoe, I., Andersen, M., Béguelin, P., Biggin, A., Davies, C., Elliott, T., Engbers, Y., Fernandes, V. M., Ferreira, A., Fowler, S., Ghelichkhan, S., Koelemeijer, P., Latallerie, F., Li, A., Morgan, G., Mason, S., Myhill, B., Nowacki, A., Récalde, N., O'Malley, C., Plimmer, A., Porcelli, D., Roberts, G., Rodney, J., Shea, J., Shorttle, O., Sturgeon, W., Walker, A., Ward, J., & Wookey, J., 2024. How to assess similarities and differences between mantle circulation models and earth using disparate independent observations: Data and analysis, Zenodo, `https://doi.org/10.5281/zenodo.13960492`.

Davies, J. H., Panton, J., Altoe, I., Andersen, M., Béguelin, P., Biggin, A., Davies, C., Elliott, T., Fernandes, V. M., Ferreira, A. M. G., Fowler, S., Ghelichkhan, S., Koelemeijer, P., Latallerie, F., Li, W., Morgan, G., Mason, S., Myhill, R., Nowacki, A., Récalde, N., O'Malley, C., Plimmer, A., Porcelli, D., Roberts, G., Rodney, J., Shea, J., Shorttle, O., Sturgeon, W., Walker, A. M., Ward, J., & Wookey, J., 2025. How to assess similarities and differences between mantle circulation models and Earth using disparate independent observations, accepted for publication in *Royal Society Proceedings A* 9th May 2025, doi: 10.1098/rspa.2024.0827, available at `https://eprints.whiterose.ac.uk/id/eprint/226526/`.

Deuss, A., Redfern, S. A. T., Chambers, K., & Woodhouse, J. H., 2006. The Nature of the 660-Kilometer Discontinuity in Earth's Mantle from Global Seismic Observations of *PP* Precursors, *Science*, **311**(5758), 198–201, doi: 10.1126/science.1120020.

Flanagan, M. P. & Shearer, P. M., 1998. Global mapping of topography on transition zone velocity discontinuities by stacking SS precursors, *Journal of Geophysical Research: Solid Earth*, **103**(B2), 2673–2692, doi: 10.1029/97JB03212.

Glasgow, M. E., Zhang, H., Schmandt, B., Zhou, W.-Y., & Zhang, J., 2024. Global variability of the composition and temperature at the 410-km discontinuity from receiver function analysis of dense arrays, *Earth and Planetary Science Letters*, **643**, 118889, doi: 10.1016/j.epsl.2024.118889.

Goes, S., Cammarano, F., & Hansen, U., 2004. Synthetic seismic signature of thermal mantle plumes, *Earth and Planetary Science Letters*, **218**(3-4), 403–419, doi: 10.1016/S0012-821X(03)00680-0.

Goes, S., Yu, C., Ballmer, M. D., Yan, J., & van der Hilst, R. D., 2022. Compositional heterogeneity in the mantle transition zone, *Nature Reviews Earth & Environment*, **3**(8), 533–550, doi: 10.1038/s43017-022-00312-w.

Gu, Y., Dziewonski, A. M., & Agee, C. B., 1998. Global de-correlation of the topography of transition zone discontinuities, *Earth and Planetary Science Letters*, **157**, 57–67.

Gu, Y. J., Dziewoński, A. M., & Ekström, G., 2003. Simultaneous inversion for mantle shear velocity and topography of transition zone discontinuities, *Geophysical Journal International*, **154**(2), 559–583, doi: 10.1046/j.1365-246X.2003.01967.x.

Guo, Z. & Zhou, Y., 2020. Finite-frequency imaging of the global 410-and 660-km discontinuities using SS precursors, *Geophysical Journal International*, **220**(3), 1978–1994.

Heister, T., Dannberg, J., Gassmöller, R., & Bangerth, W., 2017. High accuracy mantle convection simulation through modern numerical methods - II: Realistic models and problems, *Geophysical Journal International*, **210**(2), 833–851, doi: 10.1093/gji/ggx195.

Houser, C., 2016. Global seismic data reveal little water in the mantle transition zone mantle phase transitions, *Earth and Planetary Science Letters*, **448**, 94–101.

Houser, C. & Williams, Q., 2010. Reconciling Pacific 410 and 660km discontinuity topography, transition zone shear velocity patterns, and mantle phase transitions, *Earth and Planetary Science Letters*, **296**(3-4), 255–266, doi: 10.1016/j.epsl.2010.05.006.

Houser, C., Masters, G., Flanagan, M., & Shearer, P., 2008. Determination and analysis of long-wavelength transition zone structure using SS precursors, *Geophysical Journal International*, **174**(1), 178–194, doi: 10.1111/j.1365-246X.2008.03719.x.

Huang, Q., Schmerr, N., Waszek, L., & Beghein, C., 2019. Constraints on Seismic Anisotropy in the Mantle Transition Zone From Long-Period SS Precursors, *Journal of Geophysical Research: Solid Earth*, **124**(7), 6779–6800, doi: 10.1029/2019JB017307.

Ito, E., Takahashi, E., & Matsui, Y., 1984. The mineralogy and chemistry of the lower mantle" an implication of the ultrahigh-pressure phase relations in the system MgO-FeO-SiO 2, *Earth and Planetary Science Letters*, **67**, 238–248.

Jeffreys, H. & Bullen, K. E., 1940. Seismological Tables, Tech. rep., British Association Seismological

Committee, London.

Jenkins, J., Cottaar, S., White, R. S., & Deuss, A., 2016. Depressed mantle discontinuities beneath Iceland: Evidence of a garnet controlled 660 km discontinuity?, *Earth and Planetary Science Letters*, **433**, 159–168, doi: 10.1016/j.epsl.2015.10.053.

Keifer, I. & Dueker, K., 2019. Testing the hypothesis that temperature modulates 410 and 660 discontinuity topography beneath the eastern United States, *Earth and Planetary Science Letters*, **524**, doi: 10.1016/j.epsl.2019.115723.

Koroni, M., Bozdağ, E., Paulssen, H., & Trampert, J., 2017. Sensitivity analysis of seismic waveforms to upper-mantle discontinuities using the adjoint method, *Geophysical Journal International*, **210**(3), 1965–1980, doi: 10.1093/gji/ggx286.

Kronbichler, M., Heister, T., & Bangerth, W., 2012. High accuracy mantle convection simulation through modern numerical methods: High accuracy mantle convection simulation, *Geophysical Journal International*, **191**(1), 12–29, doi: 10.1111/j.1365-246X.2012.05609.x.

Laske, G., Masters, G., Ma, Z., & Pasyanos, M., 2012. CRUST1.0: An Updated Global Model of Earth's Crust, in *Geophysical Research Abstracts*, vol. 14, pp. EGU2012–3743–1, EGU, Vienna, Austria.

Lawrence, J. F. & Shearer, P. M., 2008. Imaging mantle transition zone thickness with *SdS* - *SS* finite-frequency sensitivity kernels, *Geophysical Journal International*, **174**(1), 143–158, doi: 10.1111/j.1365-246X.2007.03673.x.

Lee, S.-H., Rhie, J., Park, Y., & Kim, K.-H., 2014. Topography of the 410 and 660 km discontinuities beneath the Korean Peninsula and southwestern Japan using teleseismic receiver functions, *Journal of Geophysical Research: Solid Earth*, **119**(9), 7245–7257, doi: 10.1002/2014JB011149.

Liu, Z., Li, J., & Kong, F., 2023. Topographic variations of mantle transition zone discontinuities in the Java subduction zone and adjacent regions from receiver function analyses, *Tectonophysics*, **849**, 229723, doi: 10.1016/j.tecto.2023.229723.

Maguire, R., Ritsema, J., Van Keken, P. E., Fichtner, A., & Goes, S., 2016. *P* - and *S* -wave delays caused by thermal plumes, *Geophysical Journal International*, **206**(2), 1169–1178, doi: 10.1093/gji/ggw187.

Maguire, R., Ritsema, J., & Goes, S., 2018. Evidence of Subduction-Related Thermal and Compositional Heterogeneity Below the United States From Transition Zone Receiver Functions, *Geophysical Research Letters*, **45**(17), 8913–8922, doi: 10.1029/2018GL078378.

Met Office, 2010. Cartopy: a cartographic python library with a Matplotlib interface, https://doi.org/10.5281/zenodo.1182735.

Muir, J. M. R., Zhang, F., & Brodholt, J. P., 2021. The effect of water on the post-spinel transition and evidence for extreme water contents at the bottom of the transition zone, *Earth and Planetary Science Letters*, **565**, 116909, doi: 10.1016/j.epsl.2021.116909.

Müller, R. D., Flament, N., Cannon, J., Tetley, M. G., Williams, S. E., Cao, X., Bodur, \., Zahirovic, S., & Merdith, A., 2022. A tectonic-rules-based mantle reference frame since 1 billion years ago - implications for supercontinent cycles and plate–mantle system evolution, *Solid Earth*, **13**(7), 1127–1159, doi: 10.5194/se-13-1127-2022.

Neele, F. & Regt, H. D., 1999. Imaging upper-mantle discontinuity topography usingunderside-reflection data, *Geophysical Journal International*, **137**(1), 91–106, doi: 10.1046/j.1365-246x.1999.00768.x.

Neele, F., Regt, H., & Decar, J., 1997. Gross errors in upper-mantle discontinuity topography from underside reflection data, *Geophysical Journal International*, **129**(1), 194–204, doi: 10.1111/j.1365-246X.1997.tb00949.x.

Panton, J., 2020. *Advances in using three-dimensional mantle convection models to address global geochemical cycles*, Ph.D. thesis, Prifysgol Caerdydd Cardiff University.

Panton, J., Davies, J. H., Elliott, T., Andersen, M., Porcelli, D., & Price, M. G., 2022. Investigating Influences on the Pb Pseudo-Isochron Using Three-Dimensional Mantle Convection Models With a Continental Reservoir, *Geochemistry, Geophysics, Geosystems*, **23**(8), e2021GC010309, doi: 10.1029/2021GC010309.

Papanagnou, I., Schuberth, B. S. A., & Thomas, C., 2023. Geodynamic predictions of seismic structure and discontinuity topography of the mantle transition zone, *Geophysical Journal International*, **234**(1), 355–378, doi: 10.1093/gji/ggac478.

Pasyanos, M. E., Masters, T. G., Laske, G., & Ma, Z., 2014. LITHO1.0: An updated crust and lithospheric model of the Earth, *Journal of Geophysical Research: Solid Earth*, **119**(3), 2153–2173, doi: 10.1002/2013JB010626.

Rao, B. P., Kumar, M. R., & Saikia, D., 2020. Seismic Evidence for a Hot Mantle Transition Zone Beneath the Indian Ocean Geoid Low, *Geochemistry, Geophysics, Geosystems*, **21**(7), e2020GC009079, doi: 10.1029/2020GC009079.

Revenaugh, J. & Jordan, T. H., 1991. Mantle layering from ScS reverberations: 2. The transition zone, *Journal of Geophysical Research: Solid Earth*, **96**(B12), 19763–19780, doi: 10.1029/91JB01486.

Ringwood, A. & Major, A., 1970. The system Mg2SiO4-Fe2SiO4 at high pressures and temperatures, *Physics of the Earth and Planetary Interiors*, **3**, 89–108, doi: 10.1016/0031-9201(70)90046-4.

Ritsema, J., Xu, W., Stixrude, L., & Lithgow-Bertelloni, C., 2009. Estimates of the transition zone temperature in a mechanically mixed upper mantle, *Earth and Planetary Science Letters*, **277**(1), 244–252, doi: 10.1016/j.epsl.2008.10.024.

Rochira, F. & Thomas, C., 2023. On the Importance of Using Directional Information in the Search for Lower Mantle Reflectors, *The Seismic Record*, **3**(2), 96–104, doi: 10.1785/0320220038.

Shearer, P. M. & Masters, T. G., 1992. Global mapping of topography on the 660-km discontinuity, *Nature*, **335**, 791–796.

Stegman, D. R., 2003. *Thermochemical evolution of terrestrial planets: Earth, Mars, and the Moon*, Ph.D., University of California, Berkeley, United States – California, ISBN: 9780496690626.

Stixrude, L. & Lithgow-Bertelloni, C., 2005. Thermodynamics of mantle minerals - I. Physical properties, *Geophysical Journal International*, **162**(2), 610–632, doi: 10.1111/j.1365-246X.2005.02642.x.

Stixrude, L. & Lithgow-Bertelloni, C., 2011. Thermodynamics of mantle minerals - II. Phase equilibria, *Geophysical Journal International*, **184**(3), 1180–1213, doi: 10.1111/j.1365-246X.2010.04890.x.

Stixrude, L. & Lithgow-Bertelloni, C., 2022. Thermal expansivity, heat capacity and bulk modulus of the mantle, *Geophysical Journal International*, **228**(2), 1119–1149, doi: 10.1093/gji/ggab394.

Tackley, P. J. & Xie, S., 2002. The thermochemical structure and evolution of Earth's mantle: Constraints and numerical models, in *Philosophical Transactions of the Royal Society A: Mathematical, Physical and Engineering Sciences*, vol. 360, pp. 2593–2609, doi: 10.1098/rsta.2002.1082, Issue: 1800 ISSN: 1364503X.

Tauzin, B., Waszek, L., Ballmer, M. D., Afonso, J. C., & Bodin, T., 2022. Basaltic reservoirs in the Earth's mantle transition zone, *Proceedings of the National Academy of Sciences*, **119**(48), e2209399119, doi: 10.1073/pnas.2209399119.

Thompson, D. A., Helffrich, G., Bastow, I. D., Kendall, J. M., Wookey, J., Eaton, D. W., & Snyder, D. B., 2011. Implications of a simple mantle transition zone beneath cratonic North America, *Earth and Planetary Science Letters*, **312**(1-2), 28–36, doi: 10.1016/j.epsl.2011.09.037.

Van Heck, H. J., Davies, J. H., Elliott, T., & Porcelli, D., 2016. Global-scale modelling of melting and isotopic evolution of Earth's mantle: Melting modules for TERRA, *Geoscientific Model Development*, **9**(4), 1399–1411, doi: 10.5194/gmd-9-1399-2016.

Walter, M. J., 2003. 2.08 Melt Extraction and Compositional Variability in Mantle Lithosphere, in *Treatise on Geochemistry*, vol. 2, pp. 363– 394, Elsevier.

Waszek, L., Schmerr, N. C., & Ballmer, M. D., 2018. Global observations of reflectors in the mid-mantle with implications for mantle structure and dynamics, *Nature Communications*, **9**(1), 1–13, doi: 10.1038/s41467-017-02709-4.

Waszek, L., Tauzin, B., Schmerr, N. C., Ballmer, M. D., & Afonso, J. C., 2021a. Measurements of the 410 and 660 km discontinuities from global SS and PP precursors, doi: 10.31905/7M3LMG8X, ISC Seismological Dataset Repository, `https://doi.org/10.31905/7M3LMG8X`.

Waszek, L., Tauzin, B., Schmerr, N. C., Ballmer, M. D., & Afonso, J. C., 2021b. A poorly mixed mantle transition zone and its thermal state inferred from seismic waves, *Nature Geoscience*, **14**(12), 949–955, doi: 10.1038/s41561-021-00850-w.

White, W. & Klein, E., 2014. Composition of the Oceanic Crust, in *Treatise on Geochemistry*, vol. 4, pp. 457–496, Elsevier, doi: 10.1016/B978-0-08-095975-7.00315-6.

Wieczorek, M. A. & Meschede, M., 2018. SHTools: Tools for Working with Spherical Harmonics, *Geochemistry, Geophysics, Geosystems*, **19**(8), 2574–2592, doi: 10.1029/2018GC007529.

Yan, J., Ballmer, M. D., & Tackley, P. J., 2020. The evolution and distribution of recycled oceanic crust in the Earth's mantle: Insight from geodynamic models, *Earth and Planetary Science Letters*, **537**, doi: 10.1016/j.epsl.2020.116171.

Yu, C., Day, E. A., de Hoop, M. V., Campillo, M., & van der Hilst, R. D., 2017. Mapping Mantle Transition Zone Discontinuities Beneath the Central Pacific With Array Processing of SS Precursors, *Journal of Geophysical Research: Solid Earth*, **122**(12), 10,364–10,378, doi: 10.1002/2017JB014327.

Yu, Y., Gao, S. S., & Liu, K. H., 2020. Topography of the 410 and 660 km Discontinuities Beneath the Cenozoic Okavango Rift Zone and Adjacent Precambrian Provinces, *Journal of Geophysical Research: Solid Earth*, **125**(9), doi: 10.1029/2019JB019290.

Yu, Y. G., Wentzcovitch, R. M., Vinograd, V. L., & Angel, R. J., 2011. Thermodynamic properties of MgSiO3 majorite and phase transitions near 660 km depth in MgSiO3 and Mg2SiO 4: A first principles study, *Journal of Geophysical Research: Solid Earth*, **116**(2), doi: 10.1029/2010JB007912.

Zhao, L. & Chevrot, S., 2003. SS-wave sensitivity to upper mantle structure: Implications for the mapping of transition zone discontinuity topographies, *Geophysical Research Letters*, **30**(11), doi: 10.1029/2003GL017223.

Thermochemcial Prediction of Seismic Discontinuity Topography from Mantle Circulation Models: Supplementary information

REFERENCES

Waszek, L., Tauzin, B., Schmerr, N. C., Ballmer, M. D., & Afonso, J. C., 2021. A poorly mixed mantle transition zone and its thermal state inferred from seismic waves, *Nature Geoscience*, **14**(12), 949–955, doi: 10.1038/s41561-021-00850-w.

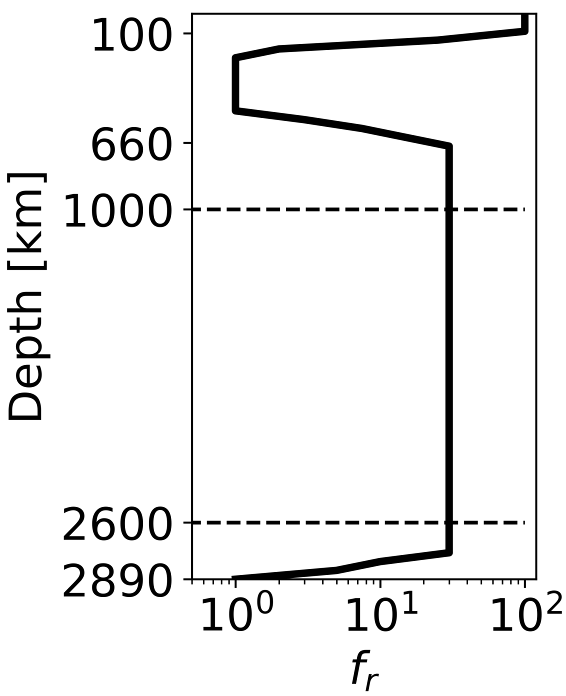

Figure S1. Variation of viscosity pre-factor with depth.

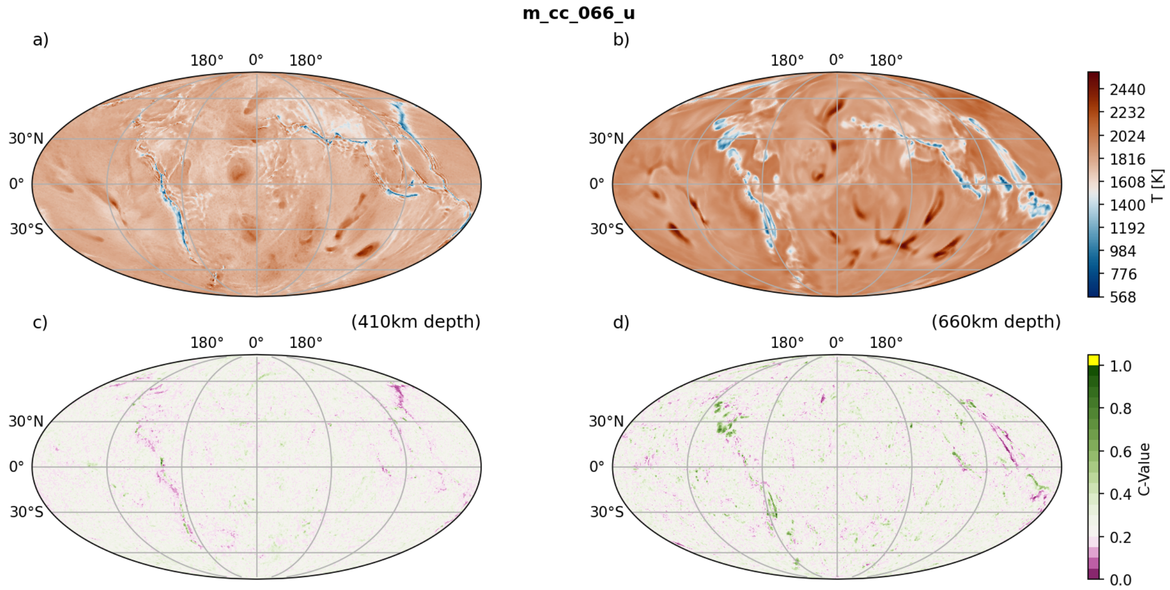

Figure S2. Thermochemical structure of simulation 'm_cc_066_u'. *a)* Thermal structure at 410 km depth *b)* C-Value structure at 410 km depth *c)* Thermal structure at 660 km depth *d)* C-Value structure at 660 km depth

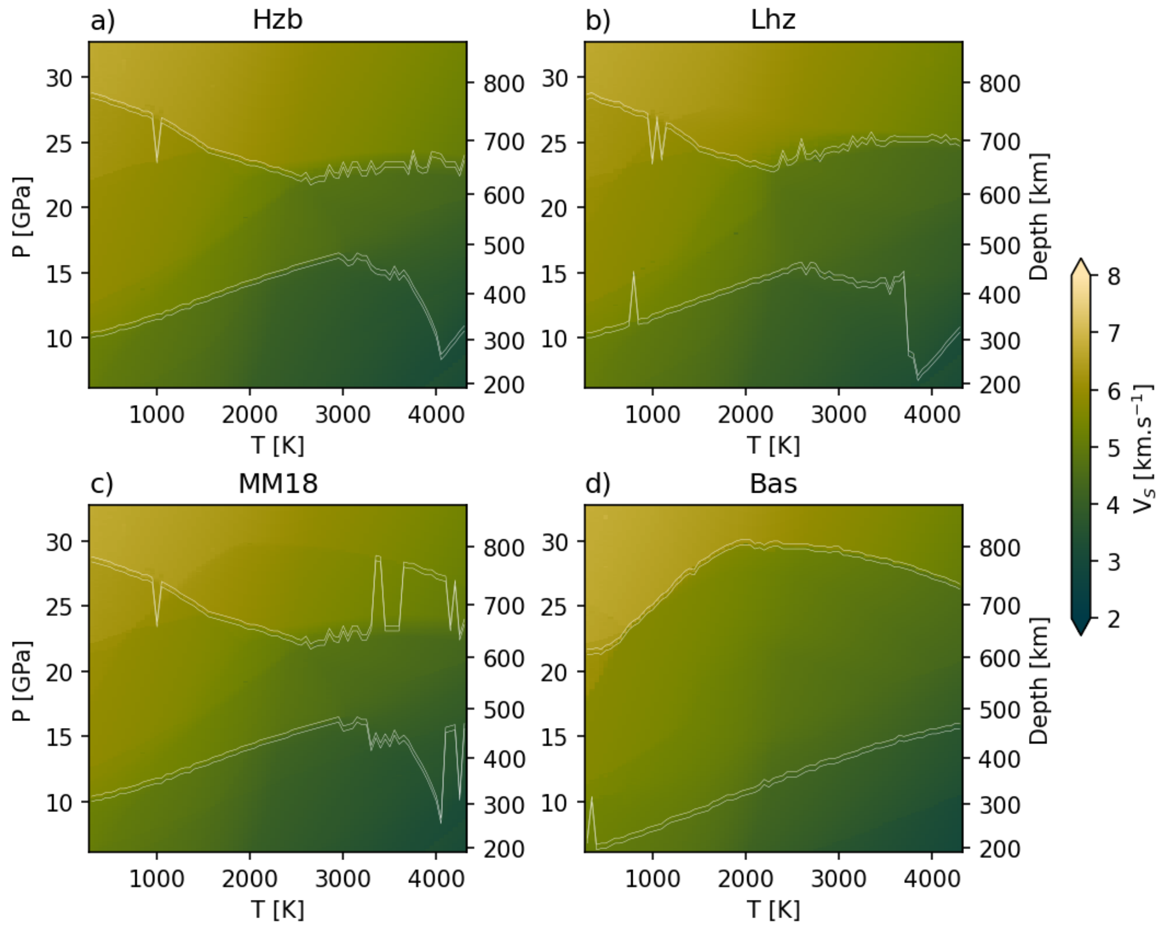

Figure S3. V_S structure of mineral physics tables for end-member compositions used in this study. *a)* Harzburgite, *b)* Lherzolite, *c)* MM18 a 'pyrolite' composition mechanical mixture of 18% Basalt and 82% Harzburgite, *d)* Basalt. V_s structure shown by color fill and the peak reflectivity pressures in the '660' and '410' regions are outlined by fine white lines 0.2 GPa above and below the picked pressure.

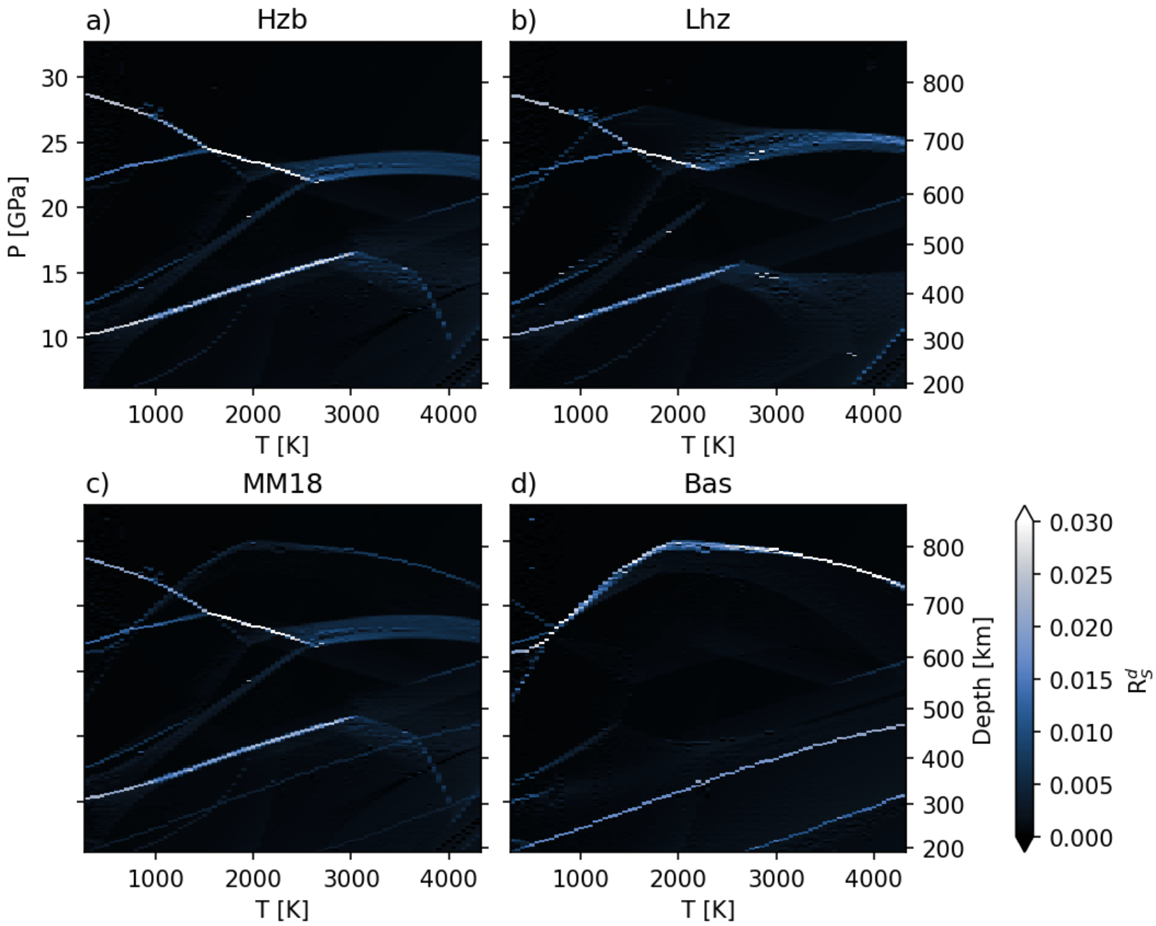

Figure S4. R_S structure of mineral physics tables for end-member compositions used in this study. *a)* Harzburgite, *b)* Lherzolite, *c)* MM18 a ‘pyrolite’ composition mechanical mixture of 18% Basalt and 82% Harzburgite, *d)* Basalt.

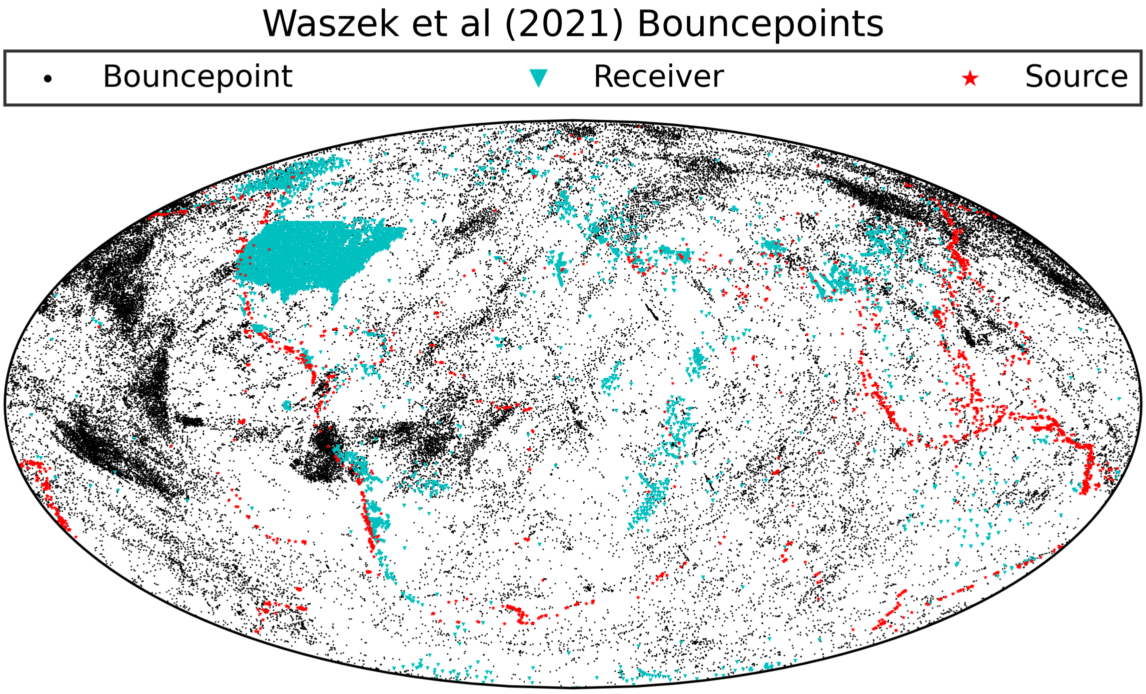

Figure S5. Distribution of seismic sources (red stars) and receivers (cyan triangles) used in Waszek et al. (2021). Bounce-points (Black dots) are then calculated as the mid-point along great circles between source-receiver pairs. Bounce-points are distributed unevenly, with clusters in the North Pacific, beneath NE Asia, Central & Eastern Europe, and Central South America.

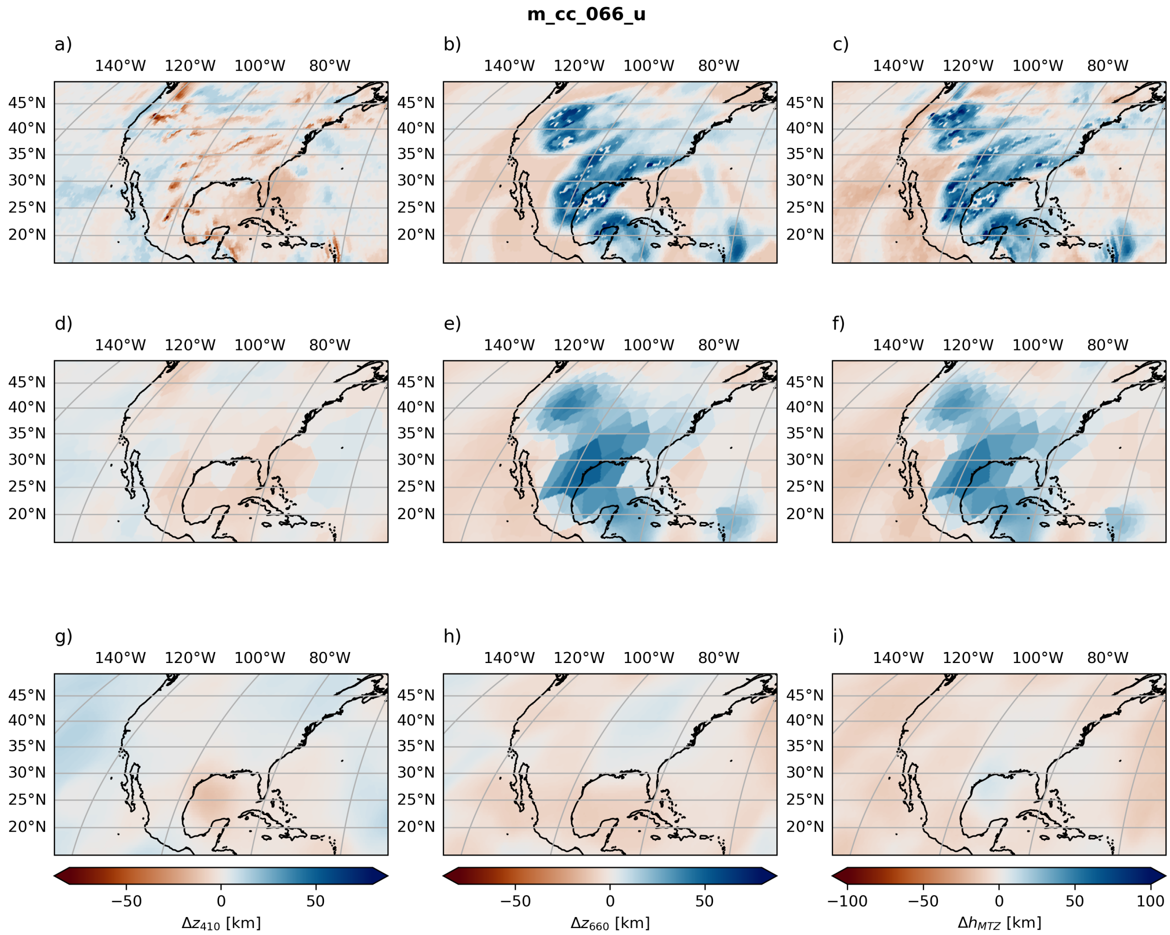

Figure S6. d410 (*a, d, g*), d660 (*b, e, h*) and MTZ thickness (*c, f, i*) topographies predicted beneath the USA and neighbouring regions from m_cc_066_u (*a–c*), predicted and filtered with a 500 km radius spherical cap (*d–f*) and the Waszek et al. (2021) model in the region (*g–i*).

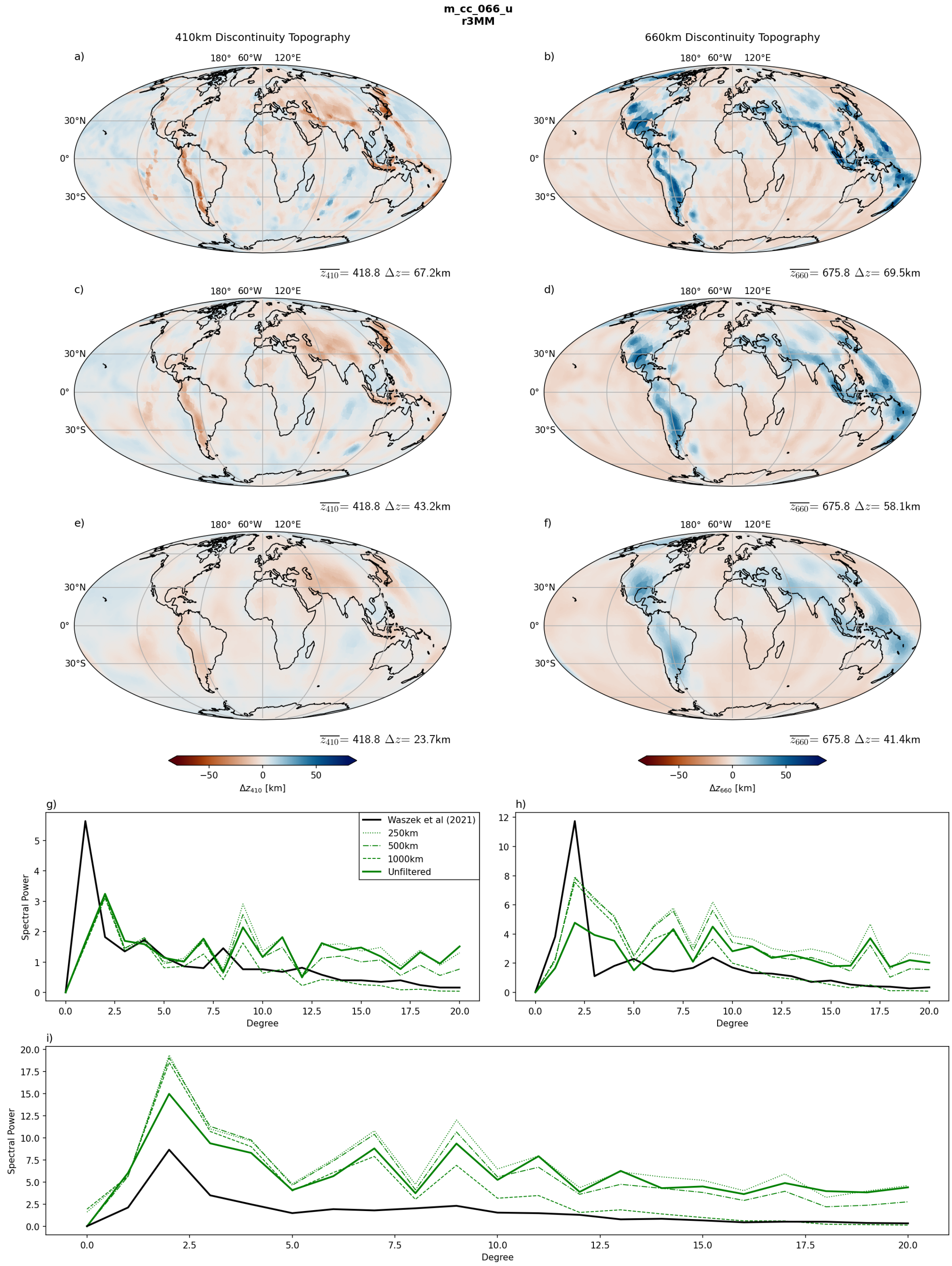

Figure S7. Variation in post-filtered topography with radius of cap used in bounce-point-spherical-cap filter. *a), c), e)* topography on 410 discontinuity with spherical cap radius 250, 500, and 1000; *km* respectively; *b), d), f)* topography on 660 discontinuity with spherical cap radius 250, 500, and 1000; *km* respectively; *g)* power spectra of 410 discontinuity with varying spherical cap radius; *h)* same as for *g*, but for 660 discontinuity. *i)* same as for g and h but for MTZ thickness

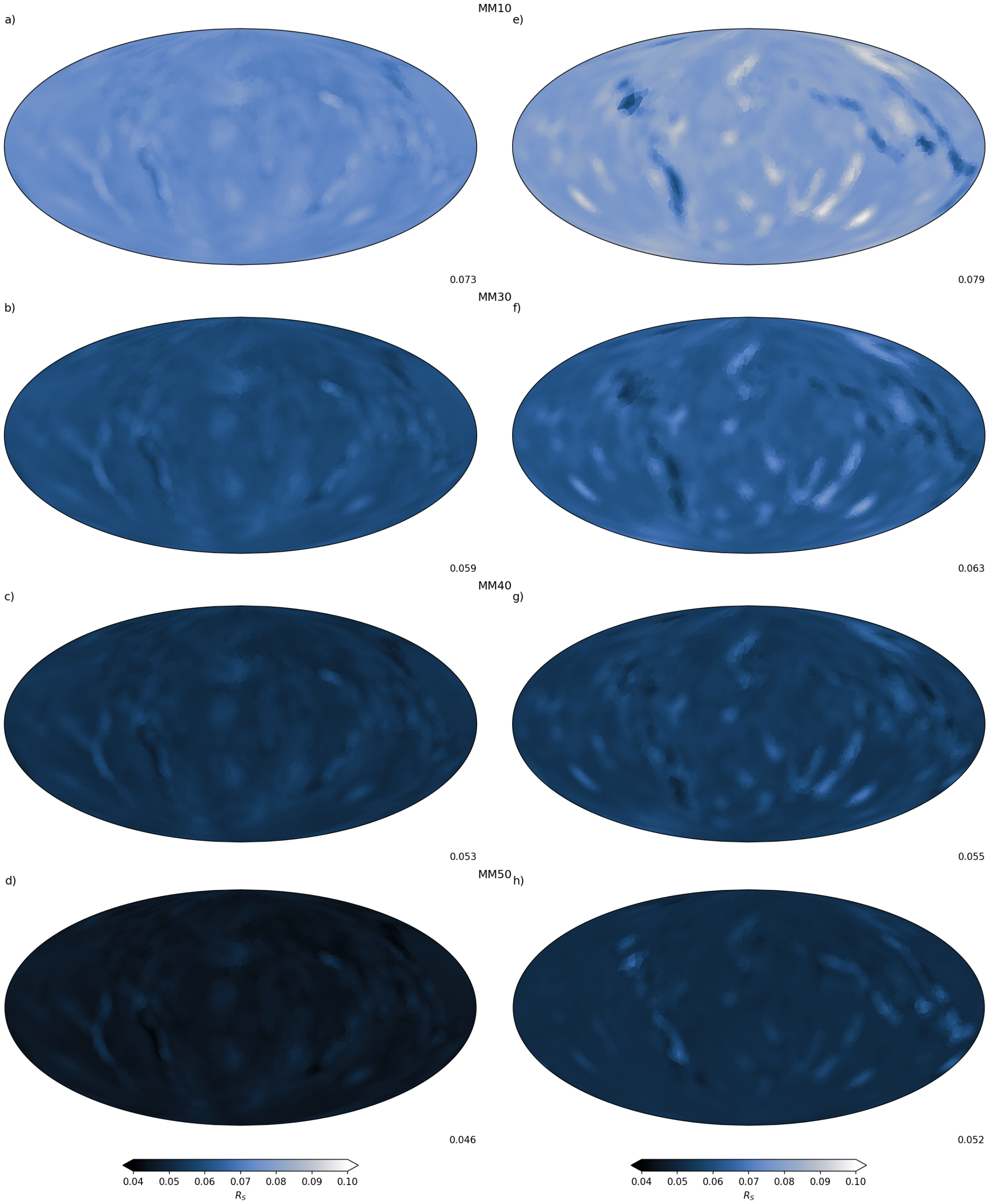

Figure S8. R_S on d410 (a–d) and d660 (e–h) for varying global mechanical mixtures MM10 (a & e), MM30 (b & f), and MM40 ((c & g) and MM50 (d and h).

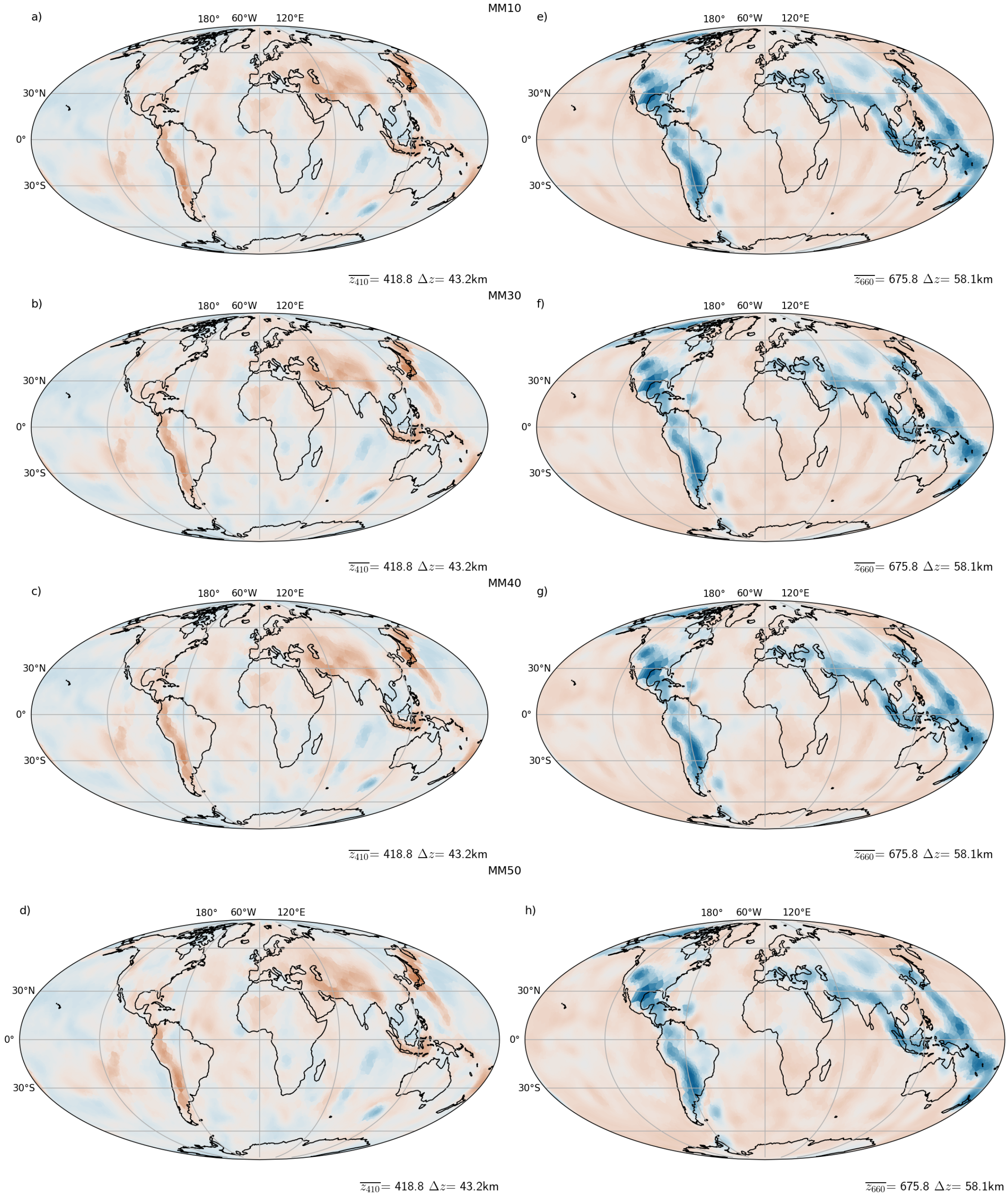

Figure S9. Filtered topography on d410 (a–c) and d660 (e–g) for varying global mechanical mixtures MM10 (a & e), MM30 (b & f), and MM40 ((c & g) and MM50 (d and h)

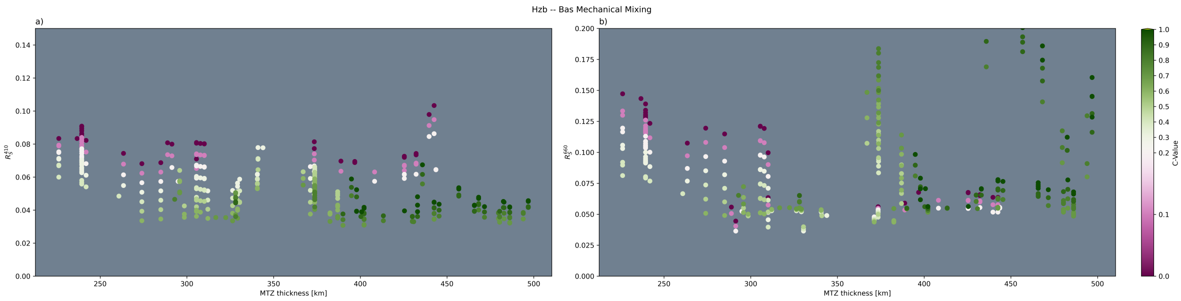

Figure S10. Relationship between R_S and MTZ thickness on *a)* d410 *b)* d660 as found from the tables used here.

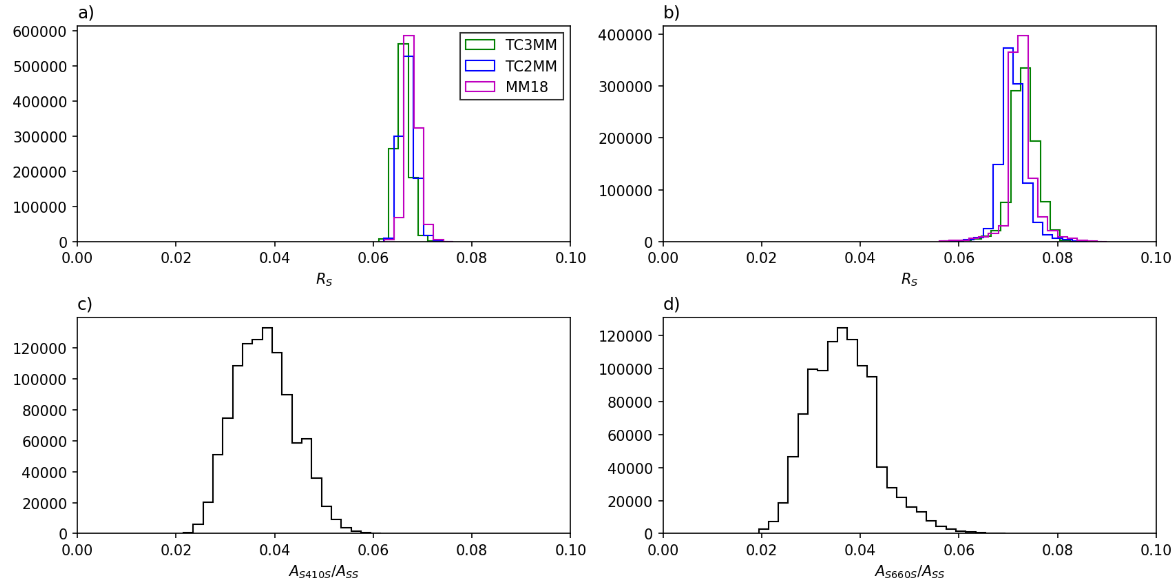

Figure S11. Histograms of *a)* R_S^{410} and *b)* R_S^{660} for the topographies predicted from the geodynamic model considered here using the local mechanical mixing assumptions and normalised SS-precursor amplitude histograms on *c)* d410 and *d)* d660 from (Waszek et al. 2021).

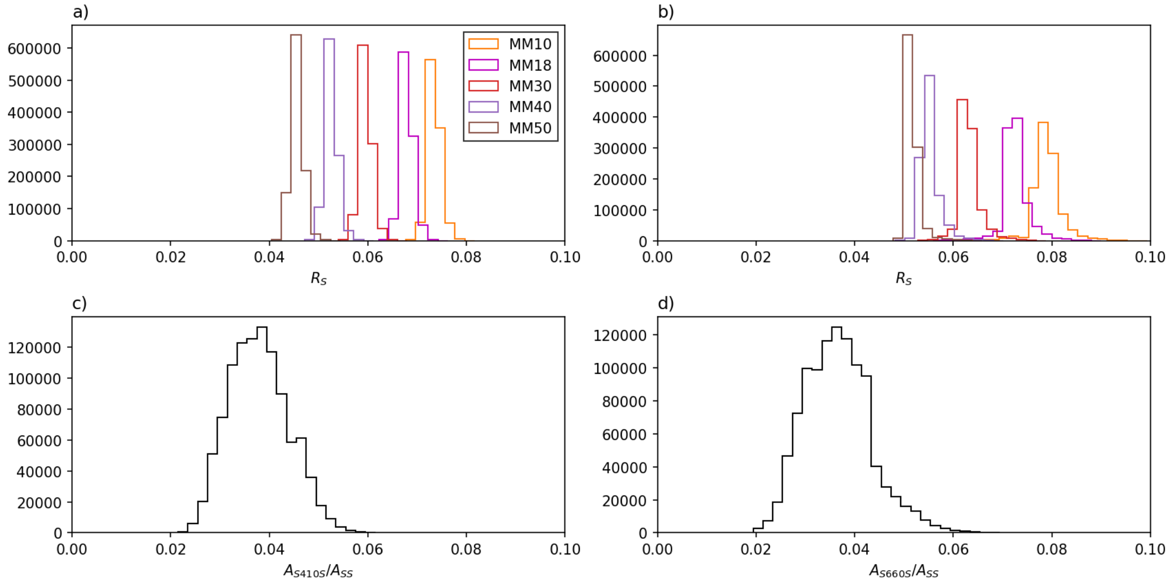

Figure S12. Histograms of *a)* R_S^{410} and *b)* R_S^{660} for the topographies predicted from the geodynamic model considered here using the different global assumed mechanical mixture compositions and normalised SS-precursor amplitude histograms on *c)* d410 and *d)* d660 from Waszek et al. (2021).